Co3O4 Nanoparticles Embedded in Mesoporous Carbon for Supercapacitor Applications

Sirine Zallouz, Bénédicte Réty, Loïc Vidal, Jean-Marc Le Meins, Camélia Matei Ghimbeu

Co_3O_4 Nanoparticles Embedded in Mesoporous Carbon for Supercapacitor Applications

Sirine Zallouz[1,2], *Bénédicte Réty*[1,2,3], *Loïc Vidal*[1,2], *Jean-Marc Le Meins*[1,2], *Camélia Matei Ghimbeu*[1,2,3,*]

[1] Université de Haute-Alsace, CNRS, Institut de Science des Matériaux de Mulhouse (IS2M) UMR 7361, F-68100 Mulhouse, France

[2] Université de Strasbourg, F-67081 Strasbourg, France

[3] Réseau sur le stockage Electrochimique de l'Energie (RS2E), FR CNRS 3459, 80039 Amiens Cedex, France

*Corresponding author

E-mail address: camelia.ghimbeu@uha.fr (C. Matei Ghimbeu).

Tel: + 33 (0) 3 89 60 87 43

ABSTRACT

Metal oxides are of great interest for supercapacitor application, however, they suffer from capacity fading during cycling and limited cycle life. In this work, a one-pot bottom-up approach is proposed to design cobalt oxide (Co_3O_4) nanoparticles confined in a mesoporous carbon. This involved the coassembly of a phenolic resin, a surfactant, and a cobalt salt followed by a high temperature pyrolysis (600−800 °C) and a subsequent low temperature oxidation (190−240 °C) step. Very small Co_3O_4 particle size (2.3−7.4 nm) could be achieved for high loadings of Co_3O_4 (up to 59%) in the carbon network. Both the pyrolysis and oxidation temperature increase led to an increase of nanoparticle size, porosity and electronic conductivity. At low temperatures, i.e., 600 and 650 °C, and despite the low particle size, the performances are poor and limited by the carbon low electronic conductivity. At high temperature (800 °C), the conductivity is improved translating in a higher capacitance, but the larger and more aggregated nanoparticles induced low rate capability. The best compromise to maintain high capacitance and rate capability was observed at 700 and 750 °C and thus for composite materials combining simultaneously dispersed nanoparticles, high porosity, and good electronic conductivity. In particular, the material treated at 750 °C presents, in a 2 electrode system using 2 M KOH, a capacitance of 54 F g^{-1} at 0.1 A g^{-1}, a very high rate capability of 48.7% at 10 A g^{-1}, and a superior rate performance of 82% after 10000 cycles.

KEYWORDS : Nanoparticles ; cobalt oxide ; carbon composites ; supercapacitor ; pseudocapacitance

1. INTRODUCTION

The growth of the global economy leads to increasing the fossil fuel consumption and this have two major consequences. The first one is the acceleration of depletion of fossil fuel resources and the second one concerns environmental problems induced by the increase of greenhouse emissions and the pollution of water and air. All of this contributes to the necessity to develop alternative, clean, and sustainable sources of energy and to investigate new technologies to store this energy. In this context, batteries and supercapacitors are the most used devices for energy storage. [1] Electrochemical supercapacitors aroused a particular interest in energy storage field owing to their ability to quickly store and release large amount of energy. This exceptional speed is explained by surface reactions of the electrode materials that do not require ion diffusion into the bulk of the materials. Another interest lies in their long life cycle with respect to the batteries. [2] Therefore, they are good candidates for applications such as electric vehicles, consumer electronic devices, military equipment, and power backup systems. Nevertheless, what hinders their use at larger scales is the poor density of energy.

Electrochemical capacitors can be classified according to their charge/discharge mechanism in two main categories, i.e., electrical double layer capacitors (EDLC) that operate by the accumulation/diffusion of charges at the interface of the electrode and the pseudocapacitors that store charge via highly reversible faradaic reactions in the electrode material. For EDLC, carbon has been the main electrode material for decades, [3−6] while the most used electrodes in pseudocapacitors are the transition metal oxides MnO_2, [7] RuO_2, [8] Fe_2O_3, [9] NiO, [10] and V_2O_5. [11] The metal oxides have shown promising results in the past years due to their high capacitance [12−14] compared to carbon. Although RuO_2 presents great performance, its exploitation is limited due to its high price. That is why other oxides such as Co_3O_4 were studied as a good alternative, thanks to its very high theoretical capacitance, its better electronic conductivity, and its lower cost. However, the major drawback of Co_3O_4 is related to the poor cyclability and structural rigidity due to the swelling and shrinking during cycling.

In order to encompass this drawback, nanostructuration of cobalt oxide has been foreseen as an interesting alternative. Numerous morphologies on the nanoscale have been synthesized such as nanosheets, [15] nanowires, [16] nanocrystals, [17] and nanoarrays. [18] Nano-Co_3O_4 materials doped with other elements like cadmium [19,20] and nitrogen [21] and supported on nickel [22] were investigated to enhance the specific capacitance and to improve the cyclability of cobalt oxide. Another strategy is to combine cobalt based materials with porous matrix (metal organic frameworks (MOFs), carbon materials, etc.). For instance, He et al. synthesized

cobalt/nickel bimetallic nanoparticles and MOFs, as materials for asymmetric supercapacitor application. [23,24] Nevertheless, nano-Co_3O_4 materials still suffer from limited electron transport rate leading to low power density and capacity fading. In this purpose, composites made of cobalt oxide nanoparticles and carbonaceous materials have been explored as a good combination to improve the electrical conductivity, to increase the specific surface area and to limit the aggregation of metal oxides nanoparticles. [25] The capacitance could be improved via the EDLC mechanism in addition to the pseudocapacitive one. Thus, the association of carbon and cobalt oxide is very promising to achieve better performance under different testing regimes.

In this context, Edison et al. prepared carbon supported cobalt oxide nanoparticles (15 and 25 nm in size) that exhibited a capacitance of 642 F g^{-1} at 1 A g^{-1} in a three electrode cell using 2 M KOH. It is worth to mention that the performance were calculated for a mass loading of 3.5 mg cm^{-2} drop casted on nickel foam having a surface of 1 cm^2. [26] In another work, Gopalakrishnan et al. synthesized a nano- Co_3O_4/graphite composite with a particle size of 10.5 nm which delivered a capacitance of 395 F g^{-1} at 0.5 A g^{-1} in a three electrode cell configuration using 6 M KOH as electrolyte. [27] The electrode mass loading used was very low, about 1 mg cm^{-2}. Electrochemical deposition of Co_3O_4 nanoflakes on electro-etched carbon fiber by cathodic potential step was as well fabricated to achieve a capacitance of 598.9 F g^{-1} at 6.25 A g^{-1} in 1 M KOH and a retention of 94% at 31.25 A g^{-1}. [28] These performance were obtained for electrodes with very low mass loading (0.32 mg cm^{-2}). Nano-Co_3O_4/graphene composites with oxygen vacancy were reported in a three electrode cell configuration with mass of active material on the current collector (Ni foam) equal to 6.5 mg cm^{-2} and exhibited a specific capacitance of 978 F g^{-1} at 1 A g^{-1}. [29] Also, Co_3O_4 nanowires on carbon nanotubes reached a volumetric specific capacitance of 734.25 F cm^{-3} at 1 A cm^{-3} using 3 M KOH as electrolyte. [30] Another study about the influence of calcination temperature of Co_3O_4 grown over carbon cloth was undertaken and had significant impact on the morphology of the materials and their energy storage properties. [31] A temperature of 250 °C was found to be the most suited one to have the best performances. This material presented a capacitance of 605 F g^{-1} at 0.25 A g^{-1} with an electrode mass of 2 mg and a thickness of 20 μm. [31]

However, it has been pointed out that the electrode material performance evaluation should be done in a 2-electrode cell configuration to be representative for a supercapacitor device. [32] For instance, a symmetric supercapacitor of nano- Co_3O_4/bioinspired carbon using poly (vinyl alcohol) (PVA) with KOH as a gel electrolyte delivers a capacitance of 28.38 F g^{-1} at 0.1 A g^{-1}.

[33] Moreover, an asymmetric supercapacitor using 3D porous carbon/nano-Co_3O_4 and activated carbon as positive and negative electrode, respectively, provided a capacitance of 60.7 F g^{-1} at 1 A g^{-1} using 3 M KOH in a voltage window of 1.6 V. [34] Nevertheless, in all these reported studies, several important aspects must be underlined. First, the mass loading is very low (less than 10 mg cm^{-2}), and the tests are done generally in three electrode cells, which might overestimate the performances. Furthermore, the amount of cobalt oxide in the carbon-based composites is usually not mentioned, and the capacitance calculation is not clearly expressed (mass of electrode or mass of Co_3O_4). Moreover, there is a lack of knowledge regarding the size of the prepared cobalt oxide particles, and when available, the values are larger than 10 nm. Hence, no systematic study to address the impact of ultrasmall nanoparticles (less than 10 nm) on the supercapacitor performances was yet reported to our knowledge. A smaller size can ensure a faster electronic diffusion, and possibly, redox reactions different from those of the bulk state might be achieved.

Therefore, this paper aims to synthesize a family of carbon/ Co_3O_4 nanocomposites possessing tunable metal oxide nanoparticles sizes in order to study their impact on the electrochemical performance. Thus, we developed a one-pot confinement strategy which allowed obtaining nano-Co_3O_4/ carbon composites with homogeneously distributed Co_3O_4 particles within the nanoscale range (1−9 nm) by varying the pyrolysis/oxidation temperature conditions. The composites revealed similar nano-Co_3O_4 loadings but distinct textural properties, surface chemistries, nanoparticle sizes, and electronic properties. Moreover, we demonstrate the impact of these properties on the electrochemical performance. The best performance (capacitance, rate capability, and cycling ability) in the two-electrode cell configuration could be achieved for the materials treated at intermediate temperature. This behavior could be explained by the good compromise between the Co_3O_4 nanoparticle size/homogeneity and confinement as well as the composite electronic conductivity.

2. MATERIALS AND METHODS

2.1. Chemicals. Triblock copolymer Pluronic F127, polytetrafluoroethylene (60% PTFE in water), and ethanol absolute anhydrous were purchased from Sigma-Aldrich. Glyoxylic acid monohydrate (98%) and phloroglucinol (>99%) were purchased from Alfa Aesar. Cobalt acetate tetrahydrate salt $(CH_3COO)_2$ $Co.4H_2O$ (>98%) was purchased from Strem Chemicals. Carbon black Super C65 was provided by TIMCAL. Qualitative filter paper no. 413 was purchased from VWR. All chemicals were used without further purification.

2.2. Material Synthesis. The Co_3O_4/carbon composites were synthesized by the soft-template method with the so-called evaporation induced self-assembly (EISA) process [35,36] implying the coassembly of phenolic resins (used as carbon source), a surfactant (pore and structure-directing agent), and a cobalt metal salt (as the Co source). The obtained polymer is processed in two steps. First, a thermal annealing step under inert atmosphere is used to obtain carbon/cobalt nanocomposites, which are subsequently oxidized to achieve carbon/ cobalt oxide nanocomposites. The first step is inspired from our previous works ; [37] however, herein the amount of cobalt is significantly higher (about 10 times). [38] The main advantage of this the one-pot route relies in the control of the cobalt particle size and particle size aggregation limitation via confinement in the carbon framework, i.e., in mesoporous carbon.

Eco-friendly precursors, i.e., 0.82 g of phloroglucinol (carbon precursor), 0.78 g of glyoxylic acid (cross-linker agent), and 1.6 g of Pluronic F127 (porogenic agent) were dissolved at room temperature in 40 mL of a mixture of solvents (water : ethanol in a ratio of 75:25 in vol. %) in a round-bottom flask. In parallel, 1.48 g of cobalt acetate was dissolved in 8 mL of water and then added to the first reaction mixture, followed by stirring for no longer than 30 s to avoid any precipitation of polymers. The as obtained solution was cast into Petri dishes (6 mL/dish of 10 cm in diameter) and evaporated in a fumehood for 12 h. This will permit the solvent evaporation and the self assembly of Pluronic template with the phloroglucinol−glyoxylic acid phenolic resin and metal salts. Once evaporation step was accomplished, a thermo-polymerization step was performed at 120 °C for 8 h in order to cross-link the phenolic resin and to immobilize the metal precursor inside this network. The obtained polymer/salt composite was mechanically removed and a first thermal treatment was performed under argon at 5 different temperatures (600, 650, 700, 750, and 800 °C), for 1 h and with a heating rate of 2 °C min^{-1}. This step allows the decomposition of all precursors and the formation of carbon/metal composites, which are denominated as C/ Co-T (where T stands for the pyrolysis temperature). To obtain C/Co_3O_4 composites, a second thermal oxidation step is performed on the C/Co-T composites under synthetic air with a heating rate of 5 °C min^{-1}. The oxidation lasted 1 h for all composites except that treated at low temperature (600 °C), where 3 h of oxidation was necessary. The oxidation temperature of cobalt was determined by thermogravimetric analysis (TGA) and ranged between 190 and 240 °C depending on the oxidation behavior of each composite, as will be explained in the Results and Discussion. The obtained oxidized composites are named C/Co_3O_4-T, where T is the annealing temperature (this parameter was preferred instead of the oxidation temperature to facilitate the understanding).

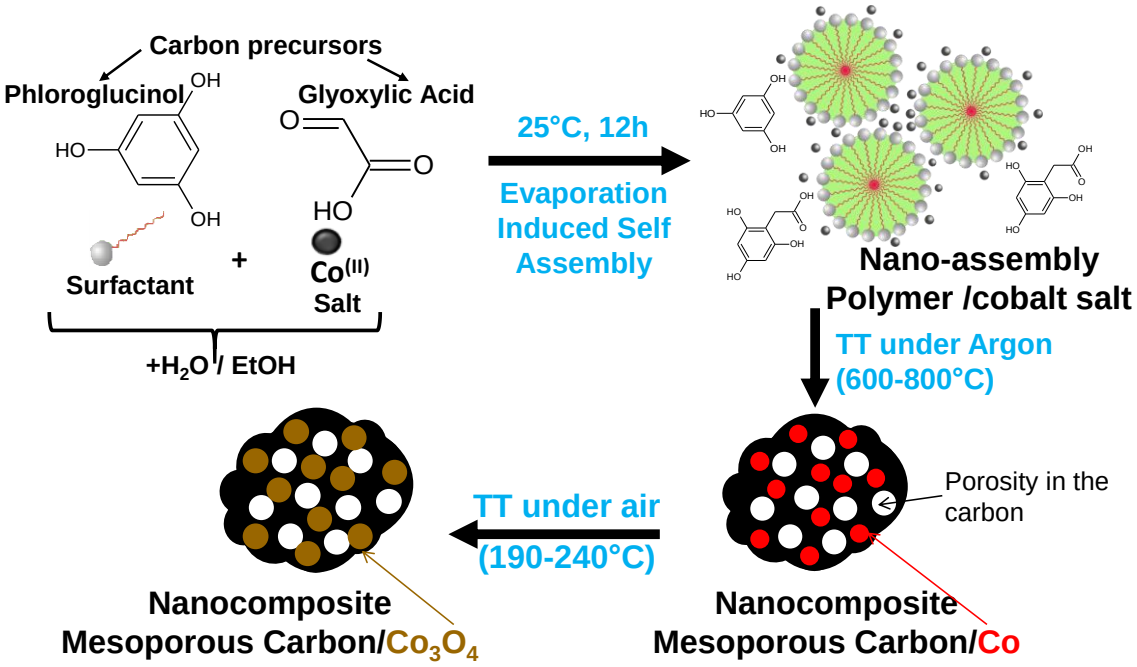

Figure 1: Schematic illustration of the one-pot synthesis of Carbon/Co_3O_4 nanocomposites.

2.3. Material Characterization. Nanocomposites were characterized by a powder X-ray diffraction system (XRD, Bruker, D8 ADVANCE A25) equipped with a LynxEye XE-T high resolution energy dispersive 1-D detector (Cu $K\alpha_{1,2}$). Data were collected and presented from 10 to 90° in 2θ. For the microstructural study, the Le Bail method [39] was used via Fullprof refinement program, [40] using a WinPlotr graphical interface. [41] Data were then converted via PowDLL [42] before treatment. A correct background is more accurately described with a polynomial function, possibly due to a slight fluorescence of cobalt, leading to better profile reliability factors. The size of the crystallites was calculated using the Scherrer formula :

$$L = \frac{K\lambda}{FWHM\ cos\theta} \quad (1)$$

Here L is the average size of ordered domains, called crystallites (nm), K is a form factor generally equal to 0.9, λ is the wavelength of X-rays (nm), FWHM is the widening of the peak at the half-maximum intensity, and θ is Bragg's angle. Thermogravimetric analysis was carried out on a Mettler Toledo instrument with a gas flow of 100 mL min^{-1}, from 25 to 800 °C at a heating rate of 2 °C min^{-1}, in an alumina (Al_2O_3) crucible. An inert atmosphere was used for the thermal precursors decomposition. Then an air atmosphere until 600 °C was used to determine the oxidation temperature of C/Co-T composites and the amount of Co_3O_4 in the composites. The surface morphology and microstructure of the samples were investigated by a transmission electron microscopy (TEM) and scanning transmission electron microscopy

(STEM) using a JEOL, ARM-200F instrument. ImageJ [43] software was used for STEM images treatment and particle size distribution by counting ~500 particles from several images. Energy dispersive X-ray (EDX) analyzer (JED 2300) was also employed to determine the chemical composition distribution of the materials. Raman technique was used to obtain additional information about the carbon/cobalt oxide composites structure. They were performed with a Raman micro spectrometer LabRAM BX40 (Horiba 300) using a wavelength of 532 nm. X-ray photoelectron spectroscopy (XPS) analyses were done on a XPS SES- 2002 (VG SCIENTA) spectrometer.

The textural properties of the nanocomposites were determined using porosimeter system ASAP 2020 from Micromeritics and N_2 as adsorbate at 77 K. Prior to the adsorption measurements, the samples (~100 mg) were placed into an analysis glass tube and outgassed under vacuum at 90 °C for 12 h on the degassing port. Furthermore, a second outgassing at 90 °C under vacuum for 2 h was performed on the analysis port. The specific surface area (S_{BET}) was calculated from the linear plot at the relative pressure range of 0.05−0.3 using the BET (Brunauer−Emmett−Teller) model. The micropore volume (V_{micro}) was determined by the Dubinin−Radushkevich (DR) equation while the mesopore volume (V_{meso}) was obtained by subtracting the micropore volume from the total pore volume (V_T) of N_2 adsorbed at relative pressure P/P_0 equal to 0.95. Pore size distribution was determined using the adsorption isotherm branch and the 2D-NLDFT (nonlocal density functional theory) standard slit pore model for carbon materials explored in SAIEUS software. [44]

2.4. Electrochemical Analysis. The electrodes were prepared by mixing 87 wt % of active material (C/Co_3O_4-T), with 10 wt % of conductive additive (carbon black SUPER C65) and 3 wt % of binder which is the polytetrafluoroethylene (PTFE), the whole dissolved in ethanol. The mixture was blended manually in a mortar until the solvent evaporated and a homogeneous paste was formed. The paste was then spread until reaching an electrode thickness of 250−300 μm. Self-standing electrodes of 10 mm diameter and 15−20 mg were cut and dried under vacuum at 120 °C for 24 h. The materials were tested in 2-electrode Swagelok cells using a symmetric configuration. All measurements were carried out in a multichannel VSP300 Potentiostat (Biologic, France). Cyclic voltammetry (CV), galvanostatic charge with potential limitation (GCPL), and electrochemical impedance spectroscopy (EIS) were conducted for 2 electrode cell assembly using 2 M KOH as electrolyte, a qualitative filter paper as separator, and stainless-steel current collectors. To further characterize the materials and see the redox peaks, a 3-electrode cell was built. In this case, Hg/HgO was used as a reference electrode, Pt mesh as counter electrode, the same electrolyte, and a gold current collector. The specific

capacitance has been calculated from GCPL using the mass of active material (carbon/Co_3O_4-T) of one electrode according to eq 2 :

$$C = \frac{2 * I * t_{dis}}{U_{max}} \quad (2)$$

Here C is the specific capacitance in F g^{-1} of active material in the working electrode, I is the applied current density in A g^{-1} of active material in the working electrode, t_{dis} is the discharge time in s and U_{max} is the electrochemical window in V.

3. RESULTS AND DISCUSSION

3.1. Materials Formation. The synthesis of carbon/ Co_3O_4 nanocomposites was performed into two distinct steps : a pyrolysis and then an oxidation. In a first step, carbon/cobalt composites were obtained via a soft-template approach involving the formation of triblock copolymer Pluronic F127 micelles and their coassembly with phloroglucinol−glyoxylic acid phenolic resin, [45] and cobalt acetate salt as depicted in Figure 1. At low temperatures (120 °C), thermo-polymerization permits the reticulation of the formed polymer, conferring a more rigid structure to immobilize the components. During the pyrolysis step at higher temperatures (up to 800 °C), several events occurs and the thermal behavior of the polymer/cobalt acetate composite was studied by thermogravimetric analysis (TGA) under nitrogen atmosphere along with the individual phenolic resin and cobalt acetate precursors (Figure 2a−c). It can be noticed that the decomposition of cobalt acetate proceeds in different stages (Figure 2a). The two peaks close to 100 °C are related to hydration water loose from the structure, while two other peaks around 250 and 350 °C are associated with the decomposition of anhydrous cobalt acetate. [46] The first peak around 250 °C is driven by a physical change having a crystalline structure while the second one reveals the decomposition process. [46] The low temperature peaks (<350 °C) are not observed in the TGA of the phenolic resin/acetate salt composite (Figure 2b) due to the thermo-polymerization step which was pre-performed at 120 °C and led to the water removal. An intense decomposition peak is seen at nearly 300 to 350 °C (Figure 2b). In this temperature range, several processes occur ; i.e., the phenolic resin decomposes forming the carbon while the Pluronic compound decomposes to form the mesopores in the carbon network. Similar behavior has been reported elsewhere [35] and is confirmed by the TGA of the phenolic resin presented in Figure 2c. Cobalt acetate $(CH_3COO)_2Co$ decomposition takes place as well (Figure 2a) and according to the literature [47] the formation of cobalt(II) oxide and several gaseous species occurs (i.e., acetone, acetic acid, water, and carbon dioxide), as expressed by reaction R1 :

$$(CH_3COO)_2\,Co\ 4H_2O + H_2O \rightarrow CoO(s) + 0.5\ CO_2\ (g) + 4.5\ H_2O\ (g) + CH_3COOH\ (g) + 0.5\ CH_3COCH_3\ (g)\ (R1)$$

At higher temperatures (>600 °C), the formed carbon acts as a reducing agent for cobalt oxide leading to metallic Co (0) through the so-called carbo-reduction reaction described as follows: [48]

$$C + CoO \rightarrow Co(s) + CO_x\ (g)\ (R2)$$

The second step of the synthesis consists in the oxidation of the as prepared carbon/Co composites to convert it into cobalt (II,III) oxide form. To estimate the required temperature for this step, thermogravimetric analysis under air was performed for all composites (Figure 2d). This analysis is crucial for three major reasons: i.e., first it allows the determination of the optimal oxidation temperature to obtain C/Co_3O_4-T composites (limiting thus carbon burnoff), second, it permits the understanding of the interactions occurring between the carbon and the particles, and last, it indicates the Co_3O_4 yield in the prepared composites. As can be seen from Figure 2d, around 200 °C, an increase in the mass uptake takes place corresponding to the Co oxidation (eq R3) followed by rapid mass loss corresponding to carbon oxidation (burnoff). Therefore, the oxidation temperature was taken at the limit between these two processes and was found to be 190 °C for material pyrolyzed at 600 °C, 215 °C for material pyrolyzed at 650 °C, 220 °C for material pyrolyzed at 700 °C, 230 °C for material pyrolyzed at 750 °C, and 240 °C for material pyrolyzed at 800 °C. It should be highlighted that the oxidation temperatures are low compared to the literature ones, where at least a temperature of 400 °C is necessary to obtain Co_3O_4. [49] This advantage might be associated with the nanoeffect (see TEM Figure 4) that renders the oxidation efficient at lower temperatures. To better explain the phenomena behind this oxidation step, one must consider that cobalt present in the carbon structure undergoes an oxidation under an air flow and forms the desired oxide, according to eq R3:

$$Co + O_2 \rightarrow CoO + O_2 \rightarrow Co_3O_4\ (R3)$$

It can be noticed additionally from Figure 2d that the oxidation temperature tends to go higher proportionally with the annealing temperature and this can be explained by several issues. First, the carbon matrix is more structured and has less oxygen-functional groups when the temperature increases (based on the XPS data that will be discussed later). Thus, it is more resistant toward oxidation. Moreover, higher temperatures may cause a more intimate enclosure of cobalt into the carbon matrix requiring a higher temperature of oxidation. Besides, the particle size is known to play a role in oxidation processes; i.e., the smaller particles having shorter diffusion pathways are oxidized much easier than the larger ones and are more reactive as well to catalyze the carbon oxidation. As will be shown by XRD, the particles size increases

with the pyrolysis temperature. Therefore, all the factors may explain the observed increase of the oxidation temperature of Co. The other important information to be drawn from the same TGA graph is the amount of Co-species residues in all carbon/ Co composites. XRD analysis was performed on one of the TGA residues, which confirms the nano-Co_3O_4 phase formation as shown in Figure S1. Based on this information, the quantity of cobalt (II,III) oxide was determined, and the results are summarized in Table 1. This technique has been used elsewhere to determine the oxide percentage as well. [50] It is clearly noticed that the amount of nano-Co_3O_4 is very high varying from 43 to 59 wt %. In the next part, the impact of pyrolysis and oxidation temperature was studied pointedly, and diverse analyses were operated to evaluate the modification of the structure of the material (phase identification, particle size, and dispersion), texture (surface area and pore size distribution), and surface chemistry.

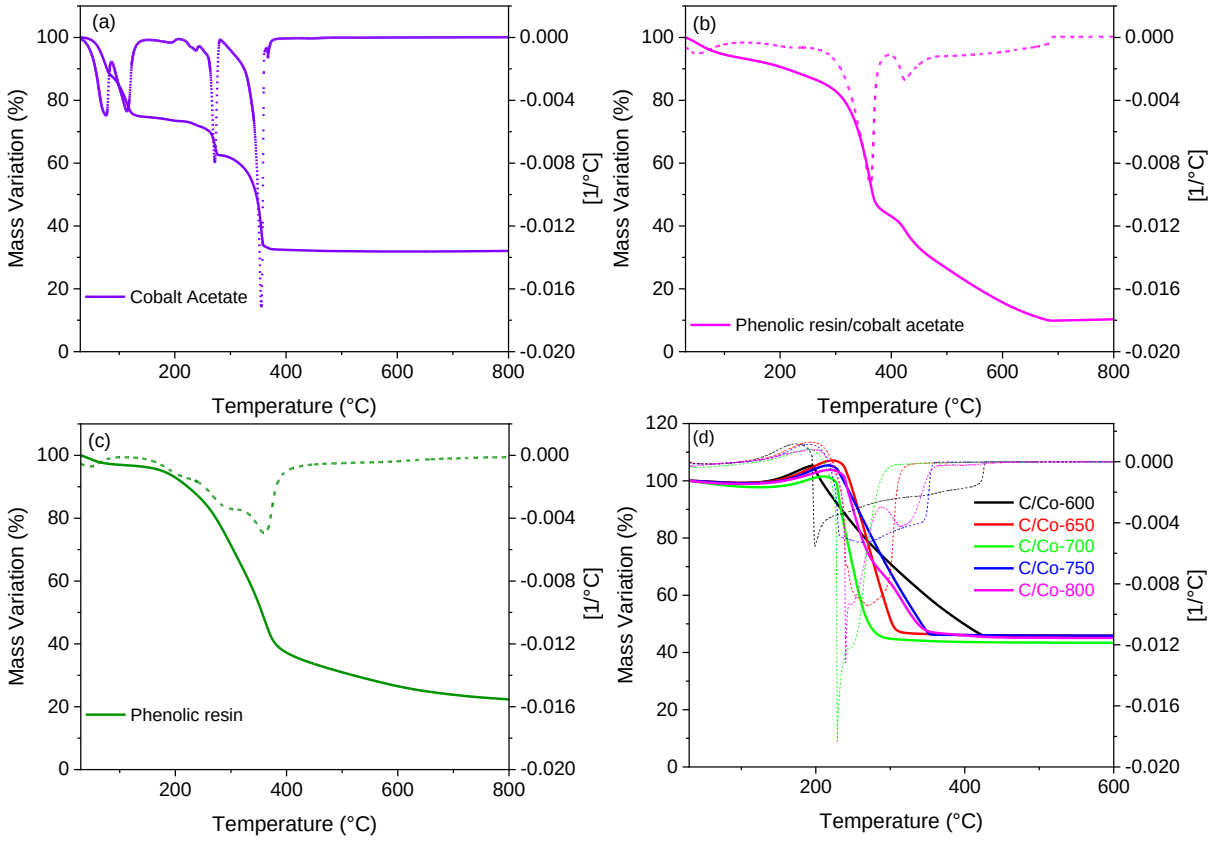

Figure 2: TGA graphs under nitrogen of (a) cobalt acetate (b) phenolic resin /cobalt acetate (c) phenolic resin and (d) under air of C/Co-T composites.

3.2. Physico-chemical Characterization. The materials structure has been evaluated via several complementary techniques, i.e., XRD, Raman and STEM, which are presented in Figure 3 and Figure 4. The XRD data (Figure 3a) show the materials obtained after the pyrolysis at different temperatures. The same phase : metallic cobalt (0) in the cubic allotropic form (PDF 00-015-0806) is observed in all the materials, in line with the formation mechanism proposed before (eq R2). The width of the peaks become narrow and may refer to an increase in the size of particles along with the thermal treatment temperature from C/Co_3O_4-600 to C/Co_3O_4-800. XRD data of C/Co composites after oxidation (Figure 3b) show the presence of several diffraction peaks. The search match process reveals the presence of Co_3O_4 phase (PDF 00-042-1467) for all materials. In particular, for C/Co_3O_4-800, a second phase is observed, which is the Co metal that did not undergo the oxidation.

The same tendency of the peak width decrease with temperature is observed : i.e., the higher the oxidation temperature, the narrower the Co_3O_4 peaks. However, this time, the mechanism is different. During the oxidation, first the oxygen is incorporated to cobalt and then the carbon is consumed. Before oxidation, the lattice parameter is 3.5447 Å, corresponding to ~6.5 unit cells of cobalt per particle (Table S1, Supporting Information) whereas after oxidation, the lattice parameter increases to 8.0837 Å, leading to only ~5.3 unit cells of Co_3O_4 per particle, proving that there is an increase. So, the narrow XRD peaks at higher temperatures underscore that the Co_3O_4 crystallites are larger. For the microstructural study, only size effects are taken into account for the profile refinement (strain effects are either too weak versus size ones or absent).

The main size results for the different compounds are summarized in Table 1. They show a global increase of the size with the oxidation temperature treatment, even if this evolution is sometimes not regular : these misfits are probably correlated to a nonunimodal size distribution. This is especially observed for C/Co_3O_4-800 (oxidized at 240 °C) that presents a clear bimodal size distribution (Figure 4f) and whose mean apparent size from XRD refinement is around 3.7 nm, whereas C/Co_3O_4-750 is a little bigger (4.3 nm). This different trend is related to the fact that C/Co_3O_4-800 has some nonoxidized Co metal, which is not taken into account for the crystallites size estimation (only Co_3O_4 XRD peaks have been used). When the particle sizes are calculated by TEM, higher values are obtained, since both Co and Co_3O_4 are counted as they cannot be distinguished based on this technique. This larger size, obtained by TEM for C/Co_3O_4-800, confirms the general increased trends of particle with the temperature.

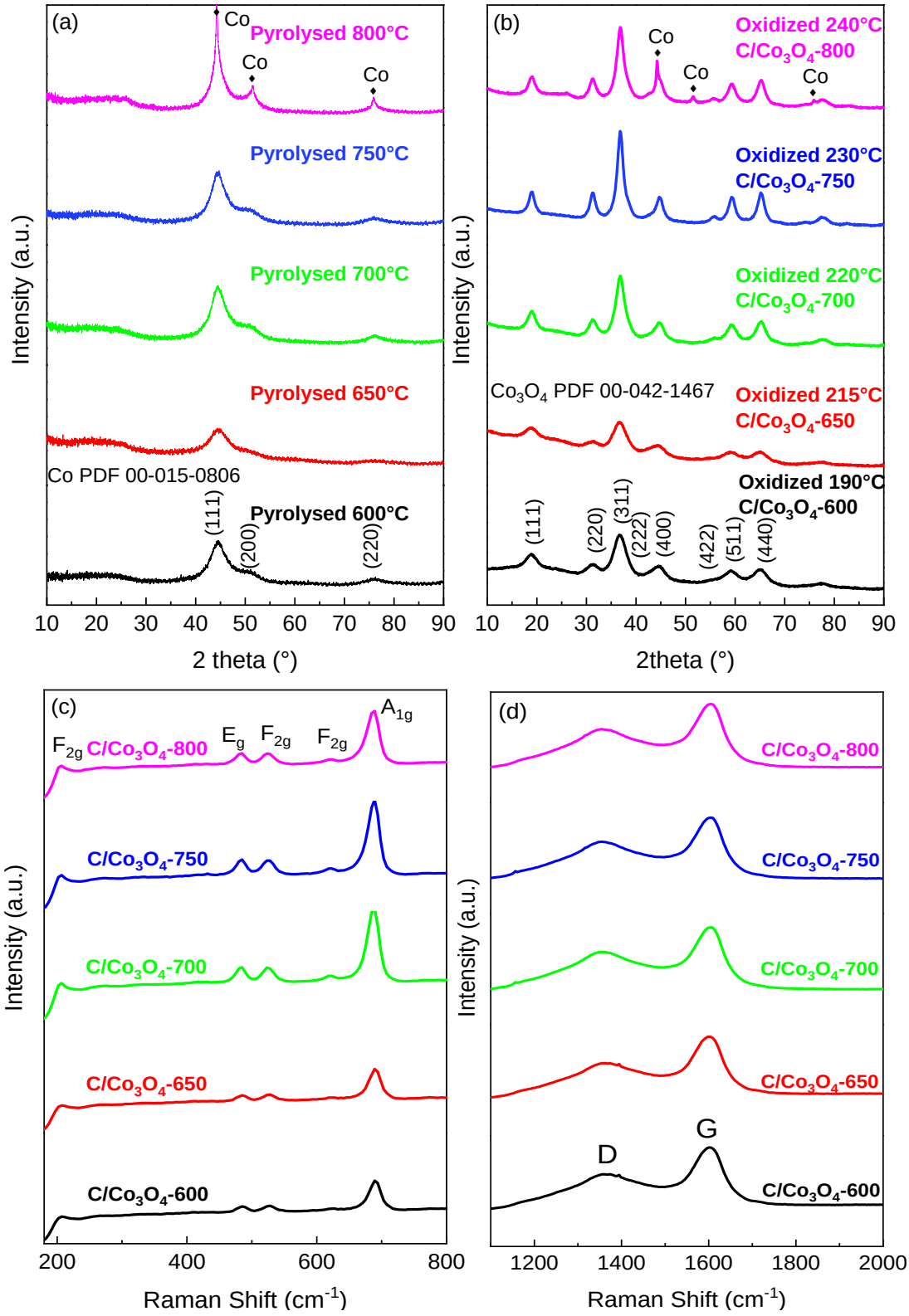

Figure 3 : XRD patterns of (a) carbon/cobalt (0)-based composites obtained by pyrolysis under argon at different temperatures and (b) the corresponding oxidized materials carbon/Co_3O_4 at different temperatures. Raman spectra of C/Co_3O_4-T composites obtained at different temperatures recorded (c) from 180 to 800 cm^{-1} and (d) from 1100 to 2000 cm^{-1}.

Raman spectroscopy (Figure 3, c and d) was performed to give more information on the materials structure. The graphs were divided in two parts in order to have a better visibility from the different Co and C contribution peaks. In the low frequency part (200−800 cm^{-1}, Figure 3c), the five peaks collected at ~197.7, 481.8, 521.8, 615.2, and 690.2 cm^{-1} correspond to the 1 A1g, 1 Eg, and 3 F2g active Raman modes of nano-Co_3O_4 in the composite, in good agreement with previous works. [51] As a general trend, an increase in the intensity for the A1g active mode (at 690.2 cm^{-1}), can be observed for the five materials and is proportional to the increase of annealing temperature and of the particles/ crystallite size, respectively. In the high frequency region (Figure 3d) two typical peaks at 1350 and 1585 cm^{-1} are displayed corresponding to D and G bands of the mesoporous carbon (MC). They are associated respectively to the structure defects and to the graphitic domains presence in the sample. [52] The integrated peak area ratio of the D and G band (I_D/I_G) is widely used to assess the structural order of carbon materials. When the temperature increases, the I_D/I_G ratio increases (Table 1) as well, and this is generated by the growth in the graphitic domains size as has been stated elsewhere. [52,53] The temperature increase favors the formation of more graphitic domains. In fact, at low temperatures (600−650 °C), the graphitic domains are very small and do not necessarily contribute in the Raman spectra whereas at high temperatures (>700 °C), the graphitic domains are larger and their contribution is better seen in the Raman spectra. [52]

HRTEM and SAED were also used to investigate the crystalline nature of the particles (Figure 4a). It can be distinguished the homogeneity of the C/Co_3O_4-700 material at smaller scale, the crystallinity of Co_3O_4 nanoparticles and some randomly oriented graphene-like planes. The selected area electron diffraction (SAED) of the same material (Figure 4b), and the fast Fourier transform (FFT) correspond to the (311), (400), (422), and (440) reticular planes of crystallized nano- Co_3O_4, previously identified in XRD diffractograms, evidencing the crystallinity of the particles. Parts d−f of Figure 4 depict STEM images along with the particles distribution of the cobalt metal nanoparticles in the C/Co composites prepared at 600, 700, and 800 °C, while parts g−i of Figure 4 present the oxidized counterpart composites at 190, 220, and 240 °C. The Co particles are very small in size, and they are remarkably homogeneously dispersed in the carbon network, despite their very high cobalt loading (~50 wt %). At 600 °C, ultra-small particles were obtained (1.1 nm) and their size tends to increase with the temperature, to 1.5 nm for 650 °C (Figure S2a, Supporting Information), 2.1 nm for 700 °C (Figure 4d), 2.3 nm for 750 °C (Figure S2b, Supporting Information), and 6.3 nm for 800 °C (Figure 4e). The increase of the

particle size is accompanied as well by some aggregations which are observed in particular for the material treated at 800 °C (Figure 4i).

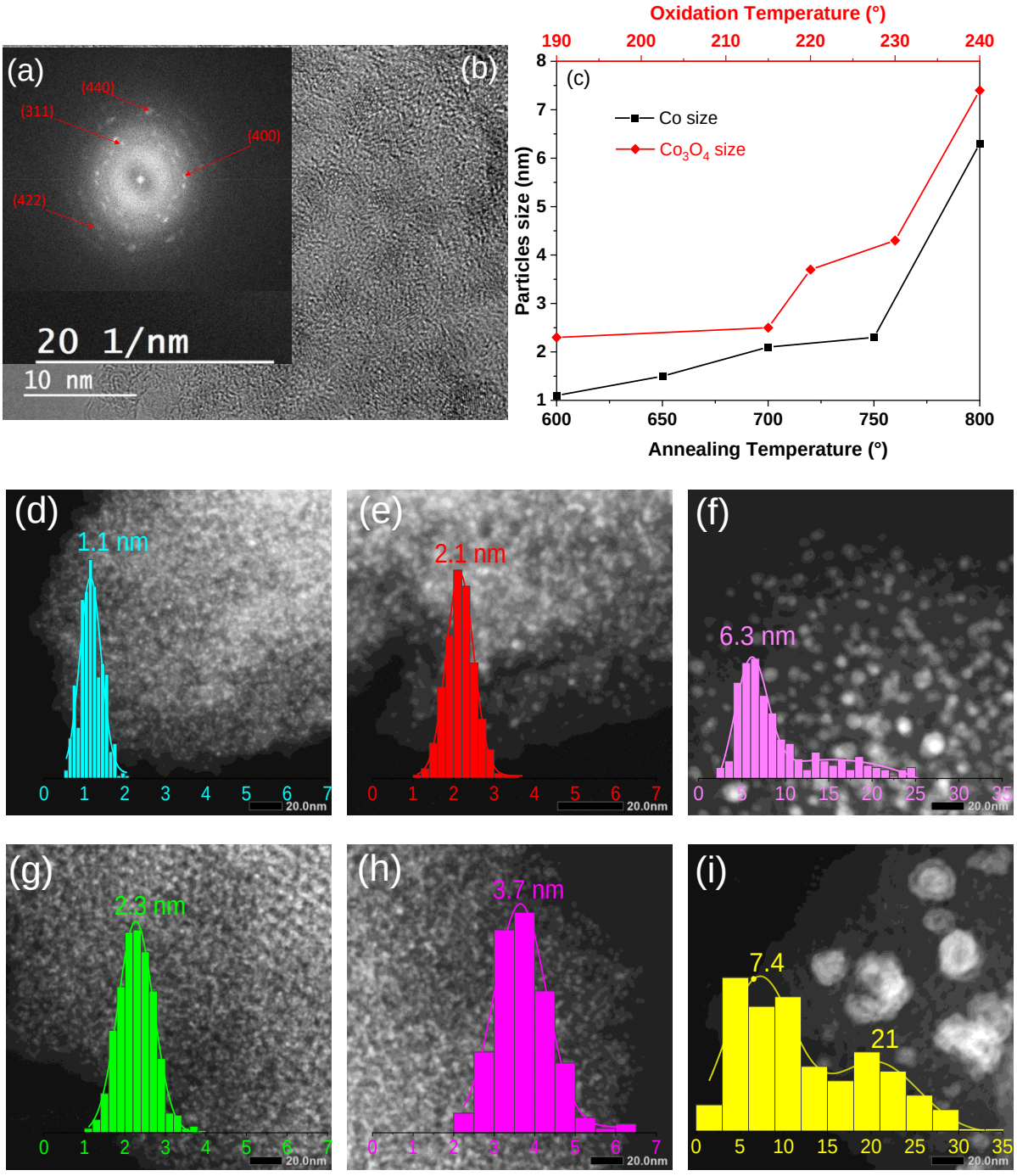

Figure 4: (a) Selected area electron diffraction (SAED) images. (b) High resolution transmission electron microscopy of C/Co_3O_4-700. (c) Evolution of particle size based on STEM analyses of C/Co composites as a function of annealing temperature and of C/Co_3O_4 as a function of oxidation temperature. STEM images of carbon/cobalt-based composites pyrolyzed at (d) 600, (e) 700, and (f) 800 °C, respectively, and the corresponding carbon/Co_3O_4 composites oxidized at (g) 190, (h) 220, and (i) 240 °C.

Overall, the composites are homogeneous, and EDX was also performed on the C/Co_3O_4-700 to see the distribution of the elements in the material and the pictures are presented in Figure S3, Supporting Information. The colored dots are present homogeneously for each element which confirms the good distribution of the particles in the material. Furthermore, EDX mapping was used to quantify the chemical composition of C, O, and Co in C/Co_3O_4-600 C/Co_3O_4-700, and C/ Co_3O_4-800 (Table S2, Supporting Information). The C content increases with the temperature from 52.1 to 78.5 wt % while the O and Co amounts decreases. This evolution can be explained by the structural reorganization of the carbon matrix and the removal of oxygen functional groups. It can be noted that a slight increase in the nanoparticles size is observed during the oxidation step for all the materials (Figure 4c).

Therefore, both the pyrolysis temperature and oxidation temperature affect the nanoparticle size. However, the pyrolysis temperature is the predominant parameter (Figure 4c). The evolution of particles size is clear as a function of the annealing and oxidation temperature. At 800 °C, a massive agglomeration especially after oxidation can be observed. This phenomenon can be explained by a thermodynamically driven spontaneous process known as the Ostwald ripening effect, where smaller particles, known to be less energetically stable, increase their tendency to join other particles leading to the formation of larger particles which are more stable. [54] Moreover, for this material, Co_3O_4 nanoparticles look like yolk-shell nanoparticles (Figure 4i), similarly as observed elsewhere. [55] This can be associated with a possible incomplete oxidation of Co as revealed by XRD. The carbon structure is also visible in some micrographs (Figure 4e), but it is not spread on the totality of the sample, showing that the obtained carbon has different structures that are rather worm-like but some hexagonal structure is observed as well (Figure 4g). The results obtained by STEM show the same particle size behavior versus temperature as the results obtained by X-ray powder diffraction. The values are in the same range and are gathered in Table 1.

Table 1: Main Characteristics C/Co_3O_4-T Composites Including Cobalt Oxide Percentage Assessed by TGA under Air, Crystallite/Particle Size Obtained by XRD and STEM, Calculations of I_D/I_G from Raman Spectra, Textural Properties Determined by Nitrogen Adsorption, and Electronic Conductivity

Material	Oxidation T(°C)	Co_3O_4 (wt %)	d XRD (nm)	d STEM (nm)	I_D/I_G	S_{BET} ($m^2\ g^{-1}$)	V_T ($cm^3\ g^{-1}$)	Vmicro ($cm^3\ g^{-1}$)	Vmeso ($cm^3\ g^{-1}$)	Conductivity ($mS\ cm^{-1}$)
C/Co_3O_4 - 600	190	43	2.6	2.3	1.40	332	0.29	0.14	0.15	0.16
C/Co_3O_4 - 650	215	57	2.7	2.5	1.41	402	0.33	0.16	0.17	0.21
C/Co_3O_4 - 700	220	52	3.1	3.7	1.76	410	0.31	0.17	0.14	0.24
C/Co_3O_4 - 750	230	59	5.2	4.3	1.73	413	0.36	0.17	0.19	0.37
C/Co_3O_4 - 800	240	52	4.2	7.4 - 21	1.72	467	0.42	0.18	0.24	0.61

The porosity of the carbon/Co_3O_4-T nanocomposites is characterized by nitrogen adsorption and the textural data are summarized in Table 1. The nitrogen adsorption/desorption isotherms and the corresponding pore size distribution for all materials are shown in Figure 5. All isotherms exhibit a type I/ IV adsorption−desorption isotherm according to IUPAC classification with a hysteresis approaching that of the H_2 type between 0.4 and 1 P/P_0 relative pressure, attesting to the mesoporous character of the materials (Figure 5a). In the low relative pressure region, there is an instant increase of adsorbed nitrogen volume testifying to the presence of micropores coming from the decomposition of the phenolic resin during thermal treatment. As a general trend, an increase in the BET specific surface area, the micropore and the mesopore volumes with the annealing temperature can be noticed. Thus, the micropore volume increases from 0.14 to 0.18 $cm^3\ g^{-1}$ while the S_{BET} increases from 332 to 467 $m^2\ g^{-1}$. This might be induced by the complete decomposition of phenolic resin and oxygen based functional groups.

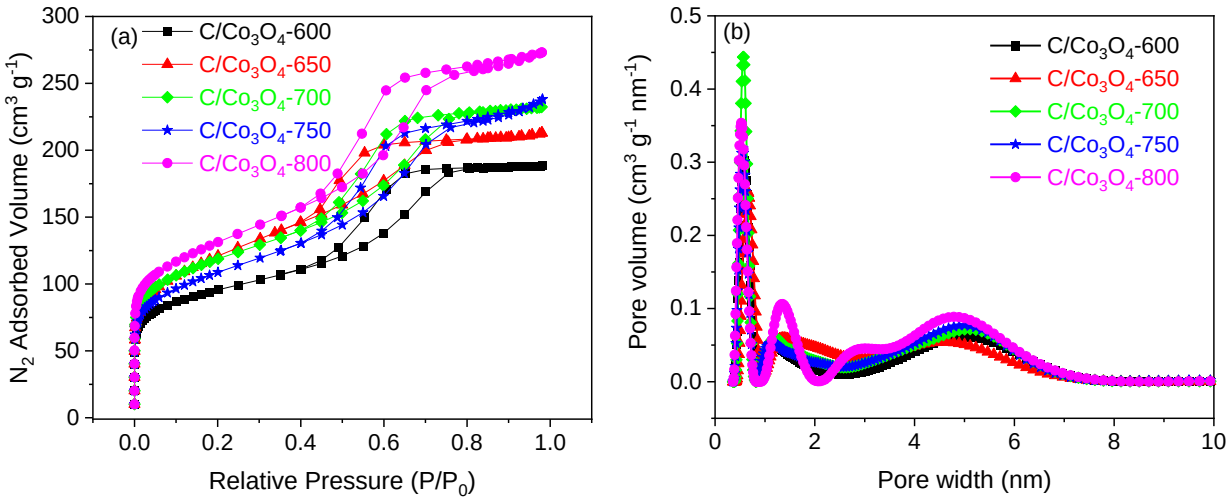

Figure 5: (a) N_2 adsorption/desorption isotherms (b) 2D-NLDFT pore size distribution of carbon/Co_3O_4 composites obtained at different temperatures.

In the same analogy, the mesoporous volume increases as well which can be more related to the emplacement and size of Co_3O_4 particles. At low temperature, the particles are small (<5 nm) and some of them are placed close to the mesopores which have the same size (~5 nm), whereas at higher temperature the particles are larger than the pores; therefore, they are more likely placed in the carbon surface. Therefore, some pores can be blocked by the particles, but a great part remains available. The materials present a similar volume of micro- and meso-pores, which is of great importance in electrochemistry. In fact, mesopores are crucial for good efficiency at high current rates as they help in electrolyte diffusion. According to some studies, the mesopores boost the capacitance retention at higher current densities as the electrolyte ions can move quicker in a mesopore, [56] while the presence of micropores allows ion storage and permits a fast ion exchange. [57] All materials present a micropore size near 0.55 nm and a less important volume of 1.5 nm as illustrated in Figure 5b. The materials present also a mesopore size of 5 nm with a wider peak. In general, the presence of two types of pores can lead to an increase of the capacitance of the materials.

The XPS technique was approached to evaluate the surface chemical composition and to confirm the chemical states of the elements by measuring their binding energy (Figures 6, S4, and S5 (Supporting Information)). The survey spectra of C/ Co_3O_4-600, C/Co_3O_4-700, and C/Co_3O_4-800 reveal the existence of the three elements, Co, C, and O, in the materials (Figure S4, Supporting Information). The high resolution deconvoluted C 1s peak (Figure 6a) illustrates the existence of a main contribution at 284.44 eV corresponding to C sp^2 and several small

contributions placed at 284.94, 286.27, 287.45, and 288.64 eV assigned to oxygen-based functional groups, i.e., C−C=O, C−OR, C=O, and COOR, respectively. [58] The shape of the peak C 1s is broader for C/Co_3O_4-600, and it gets narrower for the high temperature-treated materials. This suggest an increase in the degree of structural organization of the carbon network. [59] The tail of the C 1s peak becomes less visible as well with the increase of the temperature, which is a sign of the removal of a part of oxygen-based functional groups (from 4.9 to 8.6 at. %). The XPS O 1s deconvoluted (Figure 6b) spectra shows three peaks at 529.78, 531.40, and 533.42 eV attributed respectively the oxygen bonded to cobalt in Co_3O_4 (O−Co), to the oxygen bonded to cobalt hydroxides in $Co(OH)_2$ and also bonded on carbon (carbonyl groups, denoted C=O) and finally to the oxygen bonded to carbon (phenol groups, O−C). [22,58] The peak identified on the graph by "hydroxide, defects, and C=O" do not give quantitative information about oxygen bonded to carbon and oxygen bonded to cobalt, as only one peak is seen, and the individual peaks have close binding energy and overlap. Interestingly, the peaks related to the oxygen bonded on Co (O−Co) and oxygen bonded to carbon (O−C) present more information. The O−C peak decreases with the increase of temperature according to the peaks intensity and to the values in Table S3, Supporting Information, which varies from 4.70 to 2.96 at. %. This means that when the temperature increases less oxygen is bonded to carbon and more oxygen-bonded groups are removed. [59]

In the same time, the O−Co peak increases with the increase of temperature from 2.09 to 4.46 at. % (Table S3, Supporting Information) evidencing that a larger part of the oxygen present in the sample is coming from the cobalt oxide Co_3O_4 origin. The high-resolution spectra of Co 2p (Figure S5) show two peaks at 780.30 and 795.80 eV associated with Co $2p_{3/2}$ and Co $2p_{1/2}$, respectively, with a spin energy separation of 15.5 eV. The presence of both Co^{3+} and Co^{2+} under the curve is in good agreement with the previously reported results on Co_3O_4. [17,20] The Co content increases with the temperature from 2.68 to 6.09 at. % (Table S3, Supporting Information). This increase in the Co content with the temperature was observed by TGA as well from 43 to 52 wt % (Table 1). Primarily, this can be due to the decrease of the carbon content due to the reorganization of the structure by heteroatoms removal. Secondary, this can be also explained by the larger Co_3O_4 particles exposed more in the surface than in the carbon pore/walls for the high temperature treated samples, which therefore can be better analyzed by XPS. Moreover, the XPS chemical composition was also expressed by wt % for C/Co_3O_4-600, C/Co_3O_4-700, and C/Co_3O_4-800 (Table S2, Supporting Information). An opposite trend for C and Co amount evolution with temperature was found as compared to EDX. This difference is due to the limitations of each technique, i.e., XPS scans only the extreme surface (maximum

10 nm depth) whereas EDX is a bulk and semi-quantitative technique. A comparative graph of the two chemical compositions is provided in Figure S6, Supporting Information. In summary, the increase in the pyrolysis temperature leads to an increase of the particle size and porosity and in the same time to the removal of some oxygen-functional groups and carbon structuration. The oxidation temperature contributes also to a slight increase of the particles size, but its effect is less important than the pyrolysis temperature. The effect of these different properties on the electrochemical performance will be explored herein.

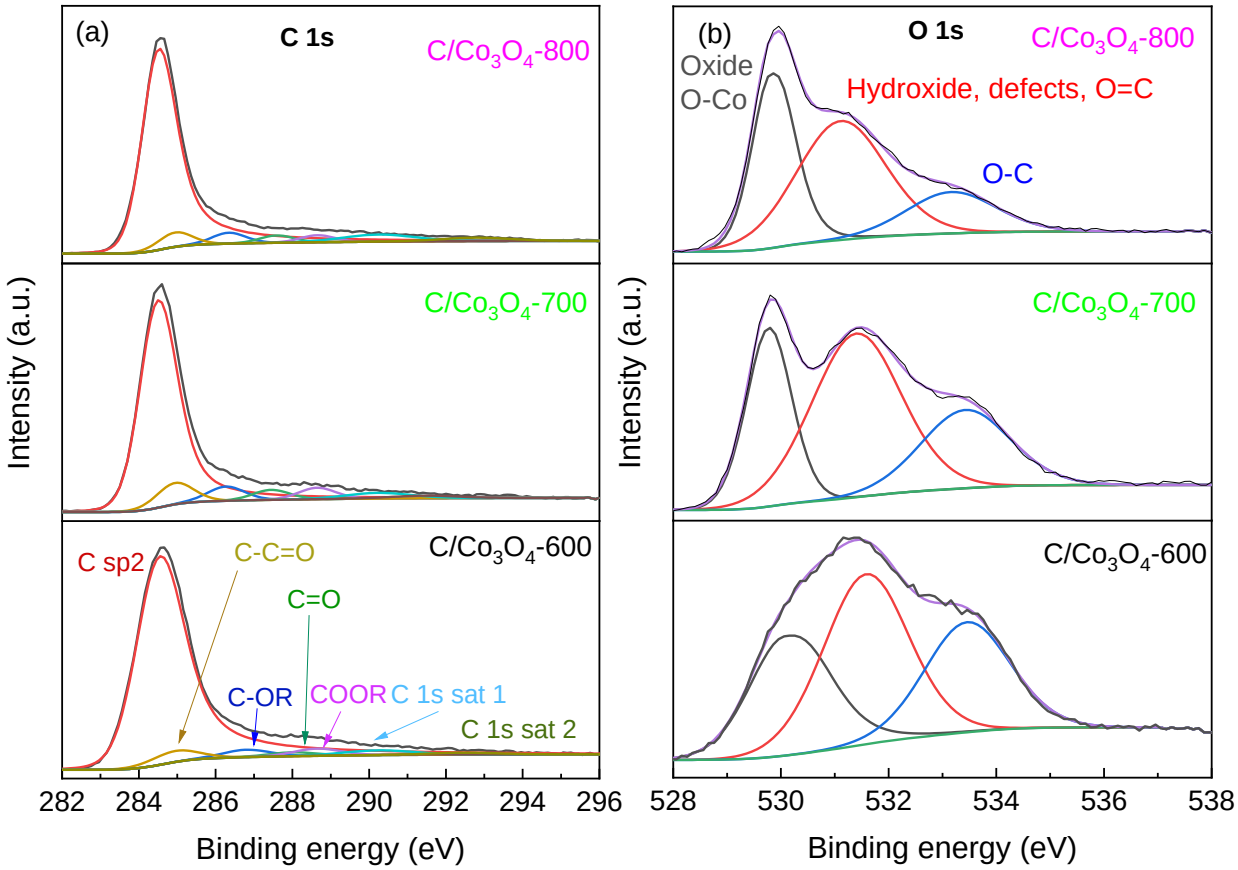

Figure 6: High resolution XPS deconvoluted spectra of (a) C 1s peak and (b) O 1s in composites C/Co_3O_4-600, C/Co_3O_4-700, and C/Co_3O_4-800.

3.3. Electrochemical Characterization. To have an understanding of the behavior of single electrodes, cyclic voltammetry (CV) in a 3-electrode system was performed to see the signature of C/Co_3O_4 materials. The measurements were performed in a potential range of −0.4 to +0.4 V vs Hg/ HgO with a scanning rate from 0.1 to 100 mV s^{-1}, as presented in Figure 7. For C/Co_3O_4-600 (Figure 7a), the redox peaks are observed for all scan rates, and there is no obvious double layer behavior, probably due to the lower specific surface area. For C/Co_3O_4-700 (Figure 7b) and C/Co_3O_4-800 (Figure 7c), the CV shape is different from C/Co_3O_4-600 material.

Progressively, the peaks are slightly hindered, their signature becomes barely distinguished and the shape is closer to a double layer behavior. This is in line with the progressive increase of the specific surface area (Table 1). In general, the redox peaks are well-defined and increase with the scanning rate, confirming that it is a faradaic pseudocapacitance. [60,61] The redox peaks are symmetric for each scanning rate proving the reversibility of the mechanism, as has been stated elsewhere. [22,29,62]

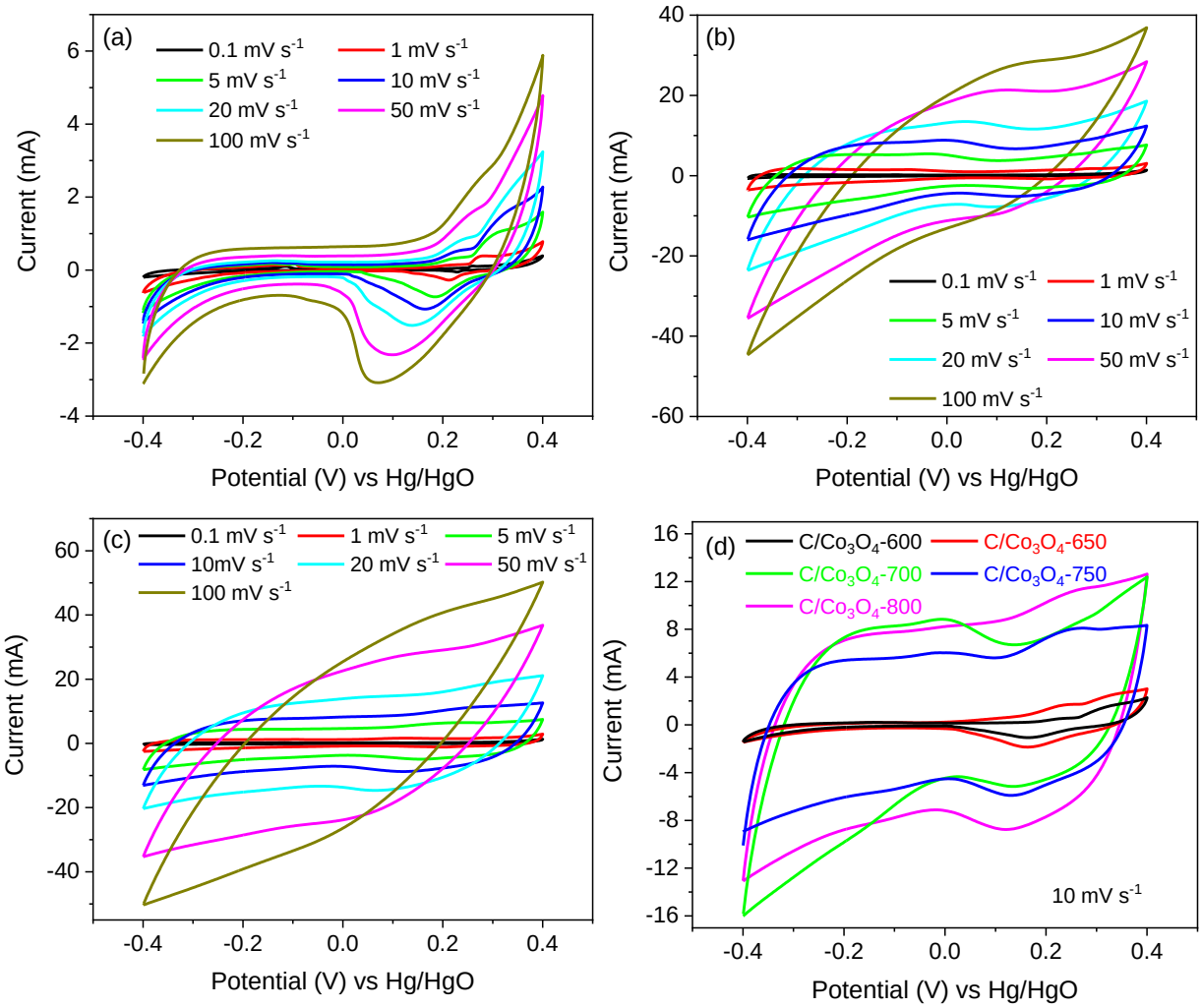

Figure 7: Cyclic voltammetry in three-electrode system at different scan rates (0.1−100 mV s^{-1}) using 2 M KOH as electrolyte for (a) C−Co_3O_4-600, (b) C−Co_3O_4-700, and (c) for C−Co_3O_4-800. (d) Cyclic voltammetry for all materials at 10 mV s^{-1}.

For a better view, Figure 7d compares the CV of all the prepared materials at 10 mV s^{-1} in three-electrode cell. As a general trend, the low temperature treated materials, i.e., C/ Co_3O_4-600 and C/ Co_3O_4-650 have limited values of current through the potential window used. The

medium temperature material C/Co_3O_4-700 and the high temperature materials C/ Co_3O_4-750 and C/Co_3O_4-800 seem to have more developed cyclic voltammograms with an EDL formation. [26,27] These different signatures can be assigned to the inner materials characteristics. With the temperature augmentation, the specific surface area and the pore volume are enhanced favoring thus the development of EDLC. Some functional groups are removed as well and the materials become more conductive, as will be shown by EIS. Aside from this, it is worth mentioning that the Co_3O_4 particle size plays a crucial role, as it increases from 2.3 to 3.7 and 7.4 nm at 600, 700, and 800 °C, respectively. Moreover, the latter material, C/Co_3O_4-800, presents some aggregations that are not present in both other materials. In fact, it is known that small particles size decrease the diffusion length; therefore, faster reactions are expected for smaller particles. [12] It has been determined that low size particles are less confined than the higher ones, and maybe more accessible, [12] which is expressed by the better defined peaks in C/Co_3O_4-700 than C/Co_3O_4-750 and C/Co_3O_4-800 (Figure 7d). Moreover, for the low treated samples, the electronic conductivity and the porosity are lower (Table 1) therefore, the pseudocapacitive behavior is more predominant. By increasing the temperature, the capacitive behavior becomes predominant and more emphasized in the voltammograms.

Several electrochemical properties were evaluated in 2-electrode system to investigate the supercapacitor application of the materials. The CV curves recorded at 10 mV s^{-1} (Figure 8a) reveal an increase of the area under the cyclic voltammograms with the increase of the annealing temperature. At lower temperatures, particularly C/Co_3O_4-600 shows the CV with the smallest area under the curve implying that its capacitance is very low. This material is not capable of forming a double layer capacitance for the reasons exposed above. As the temperature increases, the area under the curve starts to develop and the shape becomes more rectangular. This can be understood by the annealing temperature increase that leads to the carbon structural organization and the removal of oxygen based functionalities, known to be detrimental to the conductivity. [38] As a result, the carbon's electronic conductivity is improved. On the other hand, the increase in the total pore volume (both micro- and meso-pores) with the increase of the temperature (Table 1), favors the accessibility for electrolyte ions through the material. [56] The electrolyte diffusion becomes faster as well, which yields in an expansion and larger enclosed area of the CV of materials treated at the highest temperature. [56,63] For better understanding, the CV curves of C/Co_3O_4-750 measured at scan rates from 1 to 100 mV s^{-1}, in a potential window between 0 and 0.8 V are shown in Figure 8b. The shape of the cyclic voltammogram is rather rectangular with some slight signature of redox peaks. This is visible

especially at high scan rates (50 and 100 mV s^{-1}), and it implies that the capacitance is associated with a mixture of double layer (rectangular shape) and faradaic capacitance (redox peaks). According to the literature, [26,29] the anodic peak around 0.4 V for the oxidation and the cathodic peak around 0.2 V for the reduction present on a single curve correspond to the redox reactions of Co_3O_4 as follows:

$$Co_3O_4 + H_2O + OH^- \leftrightarrow CoOOH + e^- \text{ (R4)}$$

$$CoOOH + OH^- \leftrightarrow CoO_2 + H_2O + e^- \text{ (R5)}$$

The presence of the two redox peaks in a symmetric way proves that the redox processes are reversible, as highlighted elsewhere. [26,30,64,65] The galvanostatic charge−discharge (GCD) was conducted at 0.1 A g^{-1} in order to evaluate the electrochemical performance quantitatively (Figure 8c). By comparing all the materials, an increase in the efficiency is remarked with the increase of the pyrolysis temperature. This trend can be argued for many reasons: at low temperatures the discharge curve drops quickly, and the efficiency is very low; this indicates that the material does not charge electrochemically which comes probably from the limited surface area and limited electronic conductivity. Moreover, with the quick drop of discharge for low temperature treated materials, it is difficult to distinguish a clear IR drop, which is considered as an indication for internal resistance for supercapacitors. [61] Therefore, for C/Co_3O_4-600, tests performed with higher amount of conductive additive confirm the lack of conductivity since the efficiency is improved (Figure S7, Supporting Information). However, the behavior remains worse than for the other materials, suggesting indeed that other factors like the limited porosity have an impact as well.

At higher temperatures, the discharge curves are nearly symmetric to their corresponding charging counterparts, revealing good reversibility and high Coulombic efficiency, and no clear IR drop is observed. Figure 8d displays the GCD of C/Co_3O_4-750 at different current densities from 0.1 to 10 A g^{-1} and in a voltage range between 0 and 0.8 V. The charge− discharge curves are nearly symmetrical for the different current densities attesting the good reversibility of the electrochemical reactions even at higher current densities. A combination between an optimal surface area with a large pore volume divided equally between micropores and mesopores are both crucial for the good electrochemical performances. [66] Moreover, a nanoparticle size which is small, yet not aggregated, and rather well distributed in the carbon matrix, along with high ratio C sp^2/ O−C (Table S3, Supporting Information), ensures improved performance. [38]

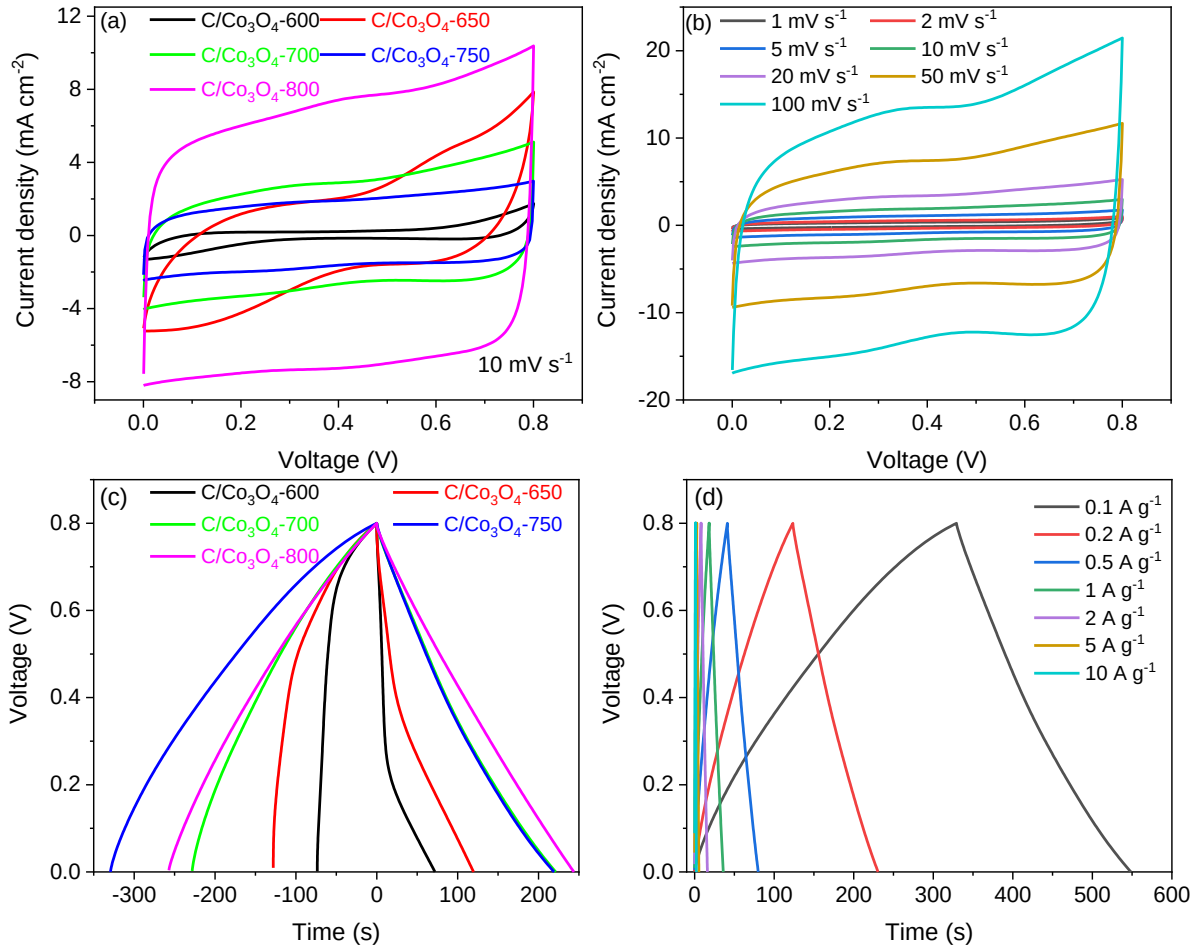

Figure 8: Electrochemical performance of 2-electrode symmetric capacitor based on C/Co_3O_4-T electrodes with 2 M KOH as electrolyte (a) cyclic voltammetry at 10 mV s^{-1} for all materials, (b) cyclic voltammetry of C−Co_3O_4-750 at different scan rates, (c) galvanostatic charging discharging with current density 0.1 A g^{-1} for all materials, and (d) galvanostatic charging discharging of C−Co_3O_4-750 at different current densities.

To get insights on the materials resistance, electrochemical impedance spectroscopy measurements were conducted from 100 kHz to 1 mHz at 0.0 and 0.8 V. The results are similar at both voltages values, thus only the results at 0.0 V are presented in Figure 9 whereas the results of EIS at 0.8 V are provided in Figure S8, Supporting Information. Figure 9a exhibits the Nyquist plot for all materials at 0.0 V. The equivalent circuit diagram is shown in the inset. Overall, a tendency of approaching the vertical line at low frequencies with the increase of the pyrolysis temperature can be noticed. C/Co_3O_4-800 has the most vertical line at low frequencies indicating a conductive and capacitive behavior, while C/ Co_3O_4-600 makes a 45° angle at low frequencies meaning the existence of a high resistance through the material. The C/ Co_3O_4-600 material exhibits the worst behavior for the three different electrochemical methods which

makes a synergy between the different results. Some half semicircles are seen at high frequency and the ESR [56] (equivalent series resistance) is similar (0.7−1.4 ohm) for all of the materials. The calculated specific capacitance values were found to be slightly higher at 0.8 V (Figure S8b) than those at 0.0 V (Figure 9b), but the difference is still negligible. Aside, there are two main trends that are observed. A line that drops quickly at low frequency values (C−Co_3O_4-600 and C/Co_3O_4-650) is typical of materials treated at lower temperatures, and a shape with a slower decrease followed by an inflection point at frequency ∼1 Hz is characteristic of materials treated at the highest temperatures. The latter behavior has been cited elsewhere as EDL capacitor behavior, [56,67,68] which can be explained by the increased porosity yielding in a faster diffusion and the higher conductivity of the carbon. The electrochemical impedance spectroscopy (EIS) has been used to determine the resistance and, subsequently, to calculate the conductivity of the materials [69] (Table 1 and Figure 9f). An increase trend of the conductivity with the pyrolysis temperature can be observed. This can be due to the improved carbon structure and the removal of oxygen in the materials. To verify the rate capability of the electrochemical devices, the specific capacitance vs current density is presented in Figure 9c. Two groups are distinguished, i.e., a group with low capacitance values and poor retention (C/Co_3O_4-600 and C/Co_3O_4-650) for the low temperature-treated materials and a group with moderate to good values with a better rate handling at 10 A g^{-1}, corresponding to high temperature treated materials.

In particular, both C/Co_3O_4-800 and C/Co_3O_4-700 have a good capacitance of 60 and 54 F g^{-1}, respectively, at a 0 1 A g^{-1} current rate. In terms of rate capability, C/Co_3O_4-750 shows the best rate handling of 48.7 % at 10 A g^{-1} owing to the optimal properties explained above. C/Co_3O_4-800 shows an interesting behavior as well, as it has the best specific capacitance at low current densities. But at 10 A g^{-1}, the retention of capacitance is only of 17.7 %, which is lower than that for C/Co_3O_4-750 and C/Co_3O_4-700. Such loss of capacitance can be explained by the material's structure containing aggregated particles (Figure 4i), known from the literature to induce poor cycling stability. [12,13,70] The high degree of confinement of Co_3O_4 in the carbon network can also limit the diffusion of the electrolyte at high current rates. An accurate comparison of the specific capacitance values with other symmetric and asymmetric devices using different type of carbon/Co_3O_4 materials is presented in Table S4, Supporting Information. It can be seen that our values are in the average of the previous reports.

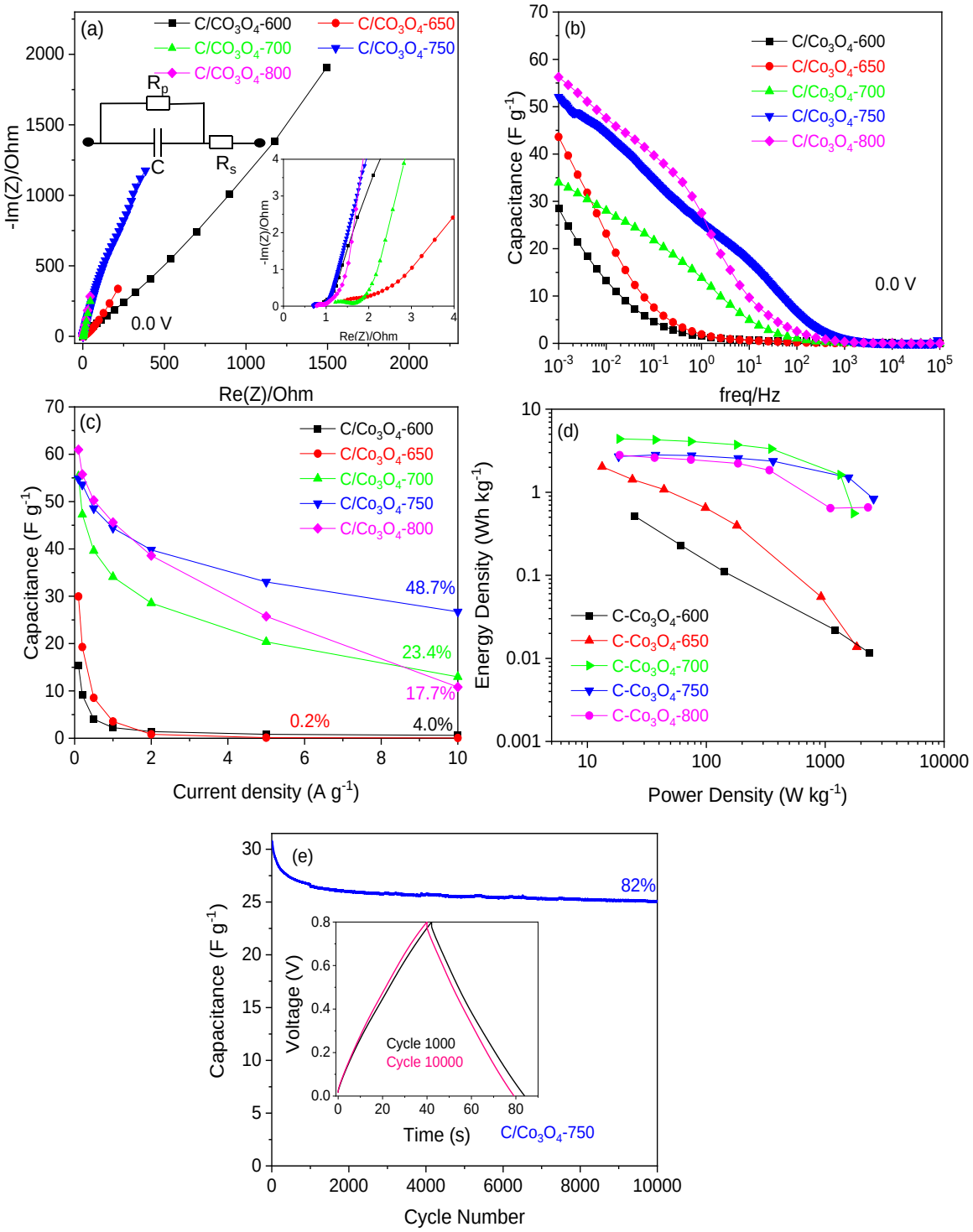

Figure 9. Electrochemical impedance spectroscopy recorded at 0.0 V for 2-electrode symmetric cells, Nyquist plot at 0.0 V (a), specific capacitance vs frequency of C/Co_3O_4-T in symmetric capacitors at 0.0 V (inset: equivalent circuit diagram) (b), specific capacitance vs current density calculated for symmetric capacitors from GCPL measurement (c), Ragone plot for the symmetric devices calculated based on the mass of active material at 0.8 V using 2 M KOH (d), and cycle life of C/Co_3O_4-750 at 0.5 A g^{-1} for 10000 cycles (e), conductivity of the C/Co_3O_4 composites using electrochemical impedance spectroscopy (f).

Based on its high capacitance and rate handling, C/Co_3O_4- 750 was selected for long cycling tests. This was performed at 0.5 A g^{-1} in a voltage window between 0.0 and 0.8 V, and the retention of the material over 10000 cycles is presented in Figure 9e. The material exhibits a high retention of 82% after 10000 cycles, which is comparable with other literature values (Table S4, Supporting Information). After a stabilization phase within the first 1000 cycles, the retention remains stable as is shown in the inset of Figure 9e, and the two GCD cycles at 1000 and 10000 are stackable. This stability in the retention over almost 9000 cycles leads us to predict that the material cycling life is longer than 10000 cycles. The energy density vs the power density is presented in a so-called Ragone plot in Figure 9d. The performance behaviors can be divided in two major families: C/Co_3O_4-600 and C/Co_3O_4-650, showing mediocre energy and power values, and then C/Co_3O_4-700, C/Co_3O_4-750, and C/Co_3O_4-800, showing significantly higher values but rather similar.

The influence of the pyrolysis temperature is clear on the materials as the increase in the temperature induces an increase in the energy density. However, C/Co_3O_4-750 and C/Co_3O_4-700 seem to present an almost constant energy vs power profile which certifies an excellent capacitive performance at high voltages. C/Co_3O_4-700 presents an energy density of 2.36 Wh kg^{-1} at a power density of 18.91 W kg^{-1} while C/Co_3O_4-750 delivers an energy density of 1.66 Wh kg^{-1} at a power density of 18.75 W kg^{-1}. Moreover, C/Co_3O_4-750 keeps a value of energy of 0.1 Wh kg^{-1} at a power of 1223 W kg^{-1}. These values are in the same range as previously reported materials summarized in Table S4, Supporting Information. However, it is worth mentioning that the mass loading of active material is not always reported or is much lower (50 μg cm^{-2} to 0.8 mg cm^{-2}) than for our materials (19−25 mg cm^{-2}), which might lead to overestimation of the performance delivered in the former cases.

As a matter of fact, this material fulfills the best compromise between the electronic conductivity, specific surface area, and metal oxide particles confinement. As underlined, all these parameters influence the performance, and moreover, they have interdependent effects. According to the different electrochemical methods employed, we can confirm that the electrochemical performance is highly influenced by the intrinsic material characteristics (structure, textural properties, functional groups, and nanoparticle size). Moreover, these different parameters interplay with each other, and the influence of one aspect is altered by another. For low temperature treated samples (600 and 650 °C), the carbon network is not yet fully developed (low porosity, high amount of oxygen-functional groups, and low

conductivity), which limits the EDLC formation. The pseudocapacitive behavior benefit coming from the nanoparticle sizes, which are observed to be very small and well dispersed in the carbon network, is limited by the low conductivity and porosity of the carbon matrix. Consequently, both the capacitance and capacitance retention at high regimes are low for these materials. For higher temperature treated samples (700−800 °C), the increase of the porosity (micro-/ meso-) and of the conductivity has a positive effect in the progressive enhancement of the EDLC and total capacitance at low regimes. Regarding the capacitance retention, this improves as well, but it reaches a maximum for the samples treated at 750 °C and then decreases again for 800 °C. This behavior difference between the 750 and 800 °C samples can be explained in terms of nanoparticle size and accessibility since the other properties (porosity and conductivity) are rather similar. In fact, the C/Co_3O_4-800 present larger and aggregated nanoparticles, and in some cases, these particles are very well confined in the carbon network and surrounded by carbon layers. Therefore, the electrolyte diffusion pathways are much longer to withstand high currents for C/Co_3O_4-800 as compared to C/Co_3O_4-750. Thus, C/Co_3O_4-750 is the composite exhibiting the best performance considering the optimal compromise between the electronic conductivity, the porosity, and the particle size/dispersion.

4. CONCLUSIONS

A one pot soft-templated synthesis route has been explored to obtain carbon/cobalt oxide nanocomposites with a very high amount of nano-Co_3O_4 in the carbon matrix (∼50−60 wt %) and a very small and well dispersed particle size. In-depth investigation of the impact of pyrolysis and oxidation temperature on the structural, textural, and surface chemistry features as well as on the energy storage properties was performed. Based on several complementary techniques, it was shown that the increase of the temperature triggers an increase of the specific surface area (332 to 467 $m^2\ g^{-1}$), and nanoparticles size (2 to 7 nm). An opposite effect of the temperature on the amount of functional groups have been observed (4.7 to 2.96 at. %).

We found that the different material properties influenced the electrochemical performances and had an interplaying effect. With the increase of temperature, the capacitive behavior, the capacitance, and the electronic conductivity increased. The C/Co_3O_4-750 presents the best performance among all materials. It exhibits in a symmetric capacitor using 2 M KOH the best specific capacitance of 54 $F\ g^{-1}$ at 0.1 $A\ g^{-1}$ and has an interestingly very good rate capability of 48.7% at 10 $A\ g^{-1}$. The same material delivers an energy density of 1.66 $Wh\ kg^{-1}$ at a power density of 18.75 $W\ kg^{-1}$. After 10000 cycles, the composite retains a high capacitance standing for 82% of its initial value. These interesting results could be explained by well-balanced

properties, i.e., texture (high specific surface area and presence of both micro- and meso-pores), small and well dispersed confined cobalt oxide nanoparticles, and good electronic conductivity. In addition, we believe that this novel synthetic route could be investigated using other metal oxide/carbon composites, which will have great potential in the energy storage field.

SUPPORTING INFORMATION

The Supporting Information is available at: https://pubs.acs.org/doi/10.1021/acsanm.1c00522. XRD pattern of the TGA residue under air of C/Co-650 composite, calculations of number of unit cells per particle before and after oxidation for a pyrolysis temperature of 750 °C, STEM images of carbon-/ cobalt-based composites pyrolyzed at 650 and 750 °C, and the corresponding C/Co_3O_4 composites oxidized at 215 and 230 °C, STEM image of C/Co_3O_4-700 composite along with the EDX mapping, Chemical composition derived from EDX and XPS for selected materials, XPS survey spectra of C/Co_3O_4 composites pyrolyzed and oxidized at different temperatures, chemical composition derived from XPS of C/Co_3O_4-600, C/Co_3O_4-700, and C/Co_3O_4-800 composites, XPS high resolution deconvoluted spectra of Co 2p peaks in C/Co_3O_4-600, C/Co_3O_4-700 and C/Co_3O_4-800 composites, chemical composition wt. (%) by (a) XPS and (b) EDX of C, O and Co for selected materials, capacitance vs current density of C/Co_3O_4-600 with different amounts of carbon black, electrochemical impedance spectroscopy recorded at 0.8 V for symmetric cells, and comparison of the performance of different carbon/Co_3O_4 materials as supercapacitor

ACKNOWLEDGMENTS

The authors thank the Université de Haute Alsace (UHA) for the financial support of this work and the laboratory of excellency for electrochemical energy storage, STORE-EX. We also thank Dr. Philippe Fioux for XPS analysis via IS2M technical platforms.

REFERENCES

(1) Simon, P.; Gogotsi, Y.; Dunn, B. Where Do Batteries End and Supercapacitors Begin? Science 2014, 343, 1210−1211.

(2) Conway, B. E. Electrochemical Supercapacitors: Scientific Fundamentals and Technological Applications; Springer Science & Business Media: 2013.

(3) Eftekhari, A.; Fan, Z. Ordered Mesoporous Carbon and Its Applications for Electrochemical Energy Storage and Conversion. Mater. Chem. Front. 2017, 1, 1001−1027.

(4) Zhang, X.; Samori, P. Graphene/Polymer Nanocomposites for Supercapacitors. ChemNanoMat 2017, 3, 362.
(5) Frackowiak, E.; Béguin, F. Carbon Materials for the Electrochemical Storage of Energy in Capacitors. Carbon 2001, 39, 937−950.
(6) Béguin, F.; Presser, V.; Balducci, A.; Frackowiak, E. Carbons and Electrolytes for Advanced Supercapacitors. Adv. Mater. 2014, 26, 2219−2251.
(7) Long, X.; Zeng, Z.; Guo, E.; Shi, X.; Zhou, H.; Wang, X. Facile Fabrication of All-Solid-State Flexible Interdigitated MnO_2 Supercapacitor via in-Situ Catalytic Solution Route. J. Power Sources 2016, 325, 264−272.
(8) Chen, L. Y.; Hou, Y.; Kang, J. L.; Hirata, A.; Fujita, T.; Chen, M. W. Toward the Theoretical Capacitance of RuO_2 Reinforced by Highly Conductive Nanoporous Gold. Adv. Energy Mater. 2013, 3, 851−856.
(9) Li, J.; Wang, Y.; Xu, W.; Wang, Y.; Zhang, B.; Luo, S.; Zhou, X.; Zhang, C.; Gu, X.; Hu, C. Porous Fe_2O_3 Nanospheres Anchored on Activated Carbon Cloth for High-Performance Symmetric Supercapacitors. Nano Energy 2019, 57, 379−387.
(10) Sun, W.; Xiao, L.; Wu, X. Facile Synthesis of NiO Nanocubes for Photocatalysts and Supercapacitor Electrodes. J. Alloys Compd. 2019, 772, 465−471.
(11) Lee, S.-M.; Park, Y.-J.; Lam, D. V.; Kim, J.-H.; Lee, K. Effects of Annealing on Electrochemical Performance in Graphene/V_2O_5 Supercapacitor. Appl. Surf. Sci. 2020, 512, 145626.
(12) Wang, T.; Chen, H. C.; Yu, F.; Zhao, X. S.; Wang, H. Boosting the Cycling Stability of Transition Metal Compounds-Based Supercapacitors. Energy Storage Materials 2019, 16, 545−573.
(13) Mohd Abdah, M. A. A.; Azman, N. H. N.; Kulandaivalu, S.; Sulaiman, Y. Review of the Use of Transition-Metal-Oxide and Conducting Polymer-Based Fibres for High-Performance Supercapacitors. Mater. Des. 2020, 186, 108199.
(14) Borenstein, A.; Hanna, O.; Attias, R.; Luski, S.; Brousse, T.; Aurbach, D. Carbon-Based Composite Materials for Supercapacitor Electrodes: A Review. J. Mater. Chem. A 2017, 5, 12653−12672.
(15) Yang, Q.; Lu, Z.; Sun, X.; Liu, J. Ultrathin Co_3O_4 Nanosheet Arrays with High Supercapacitive Performance. Sci. Rep. 2013, 3, 3537.
(16) Xia, X.; Tu, J.; Zhang, Y.; Mai, Y.; Wang, X.; Gu, C.; Zhao, X. Freestanding Co_3O_4 Nanowire Array for High Performance Supercapacitors. RSC Adv. 2012, 2, 1835.

(17) Liu, X. Y.; Gao, Y. Q.; Yang, G. W. A Flexible, Transparent and Super-Long-Life Supercapacitor Based on Ultrafine Co_3O_4 Nanocrystal Electrodes. Nanoscale 2016, 8, 4227−4235.
(18) Liu, B.; Kong, D.; Zhang, J.; Wang, Y.; Chen, T.; Cheng, C.; Yang, H. Y. 3D Hierarchical Co_3O_4 @Co_3S_4 Nanoarrays as Cathode Materials for Asymmetric Pseudocapacitors. J. Mater. Chem. A 2016, 4, 3287−3296.
(19) Deng, S.; Xiao, X.; Chen, G.; Wang, L.; Wang, Y. Cd Doped Porous Co_3O_4 Nanosheets as Electrode Material for High Performance Supercapacitor Application. Electrochim. Acta 2016, 196, 316−327.
(20) Patil, D. S.; Pawar, S. A.; Shin, J. C. Core-Shell Structure of Co_3O_4@CdS for High Performance Electrochemical Supercapacitor. Chem. Eng. J. 2018, 335, 693−702.
(21) Lin, Z.; Qiao, X. Coral-like Co_3O_4 Decorated N-Doped Carbon Particles as Active Materials for Oxygen Reduction Reaction and Supercapacitor. Sci. Rep. 2018, 8, 1802.
(22) Guo, C.; Yin, M.; Wu, C.; Li, J.; Sun, C.; Jia, C.; Li, T.; Hou, L.; Wei, Y. Highly Stable Gully-Network Co_3O_4 Nanowire Arrays as Battery-Type Electrode for Outstanding Supercapacitor Performance. Front. Chem. 2018, 6, 636.
(23) Gao, S.; Sui, Y.; Wei, F.; Qi, J.; Meng, Q.; Ren, Y.; He, Y. Dandelion-like Nickel/Cobalt Metal-Organic Framework Based Electrode Materials for High Performance Supercapacitors. J. Colloid Interface Sci. 2018, 531, 83−90.
(24) Zhang, X.; Wang, J.; Ji, X.; Sui, Y.; Wei, F.; Qi, J.; Meng, Q.; Ren, Y.; He, Y. Nickel/Cobalt Bimetallic Metal-Organic Frameworks Ultrathin Nanosheets with Enhanced Performance for Supercapacitors. J. Alloys Compd. 2020, 825, 154069.
(25) Xiao, S.; Huang, J.; Lin, C.; Xie, A.; Lin, B.; He, L.; Sun, D. Porous Carbon Derived from Rice Husks as Sustainable Bioresources: Insights into the Role of Micro/Mesoporous Hierarchy in Co_3O_4/C Composite for Asymmetric Supercapacitors. Microporous Mesoporous Mater. 2020, 291, 109709.
(26) Edison, T. N. J. I.; Atchudan, R.; Sethuraman, M. G.; Lee, Y. R. Supercapacitor Performance of Carbon Supported Co_3O_4 Nanoparticles Synthesized Using Terminalia Chebula Fruit. J. Taiwan Inst. Chem. Eng. 2016, 68, 489−495.
(27) M, G.; G, S.; A, M.; V, A. In-Situ Synthesis of Co_3O_4/Graphite Nanocomposite for High-Performance Supercapacitor Electrode Applications. Appl. Surf. Sci. 2017, 403, 578−583.
(28) Kazemi, S. H.; Asghari, A.; kiani, M. A. High Performance Supercapacitors Based on the Electrodeposited Co_3O_4 Nanoflakes on Electro-Etched Carbon Fibers. Electrochim. Acta 2014, 138, 9−14.

(29) Yang, S.; Liu, Y.; Hao, Y.; Yang, X.; Goddard, W. A.; Zhang, X. L.; Cao, B. Oxygen-Vacancy Abundant Ultrafine Co_3O_4/Graphene Composites for High-Rate Supercapacitor Electrodes. Adv. Sci. 2018, 5, 1700659.
(30) Sun, J.; Man, P.; Zhang, Q.; He, B.; Zhou, Z.; Li, C.; Wang, X.; Guo, J.; Zhao, J.; Xie, L.; Li, Q.; Sun, J.; Hong, G.; Yao, Y. Hierarchically-Structured Co_3O_4 Nanowire Arrays Grown on Carbon Nanotube Fibers as Novel Cathodes for High-Performance Wearable Fiber-Shaped Asymmetric Supercapacitors. Appl. Surf. Sci. 2018, 447, 795−801.
(31) Rakhi, R. B.; Chen, W.; Cha, D.; Alshareef, H. N. Influence of Calcination Temperature on the Morphology and Energy Storage Properties of Cobalt Oxide Nanostructures Directly Grown over Carbon Cloth Substrates. Mater. Renew Sustain Energy 2013, 2, 17.
(32) Mathis, T. S.; Kurra, N.; Wang, X.; Pinto, D.; Simon, P.; Gogotsi, Y. Energy Storage Data Reporting in Perspective- Guidelines for Interpreting the Performance of Electrochemical Energy Storage Systems. Adv. Energy Mater. 2019, 9, 1902007.
(33) Samdani, K. J.; Kim, S. H.; Park, J. H.; Hong, S. H.; Lee, K. T. Morphology-Controlled Synthesis of Co_3O_4 Composites with Bio- Inspired Carbons as High-Performance Supercapacitor Electrode Materials. J. Ind. Eng. Chem. 2019, 74, 96−102.
(34) Li, S.; Yang, K.; Ye, P.; Ma, K.; Zhang, Z.; Huang, Q. Three- Dimensional Porous Carbon/Co_3O_4 Composites Derived from Graphene/Co-MOF for High Performance Supercapacitor Electrodes. Appl. Surf. Sci. 2020, 503, 144090.
(35) Matei Ghimbeu, C.; Vidal, L.; Delmotte, L.; Le Meins, J.-M. L.; Vix-Guterl, C. Catalyst-Free Soft-Template Synthesis of Ordered Mesoporous Carbon Tailored Using Phloroglucinol/Glyoxylic Acid Environmentally Friendly Precursors. Green Chem. 2014, 16, 3079−3088.
(36) Nita, C.; Bensafia, M.; Vaulot, C.; Delmotte, L.; Matei Ghimbeu, C. Insights on the Synthesis Mechanism of Green Phenolic Resin Derived Porous Carbons via a Salt-Soft Templating Approach. Carbon 2016, 109, 227−238.
(37) Jahel, A.; Ghimbeu, C. M.; Darwiche, A.; Vidal, L.; Hajjar- Garreau, S.; Vix-Guterl, C.; Monconduit, L. Exceptionally Highly Performing Na-Ion Battery Anode Using Crystalline SnO_2 Nanoparticles Confined in Mesoporous Carbon. J. Mater. Chem. A 2015, 3, 11960−11969.
(38) Moussa, G.; Hajjar-Garreau, S.; Taberna, P.-L.; Simon, P.; Matei Ghimbeu, C. Eco-Friendly Synthesis of Nitrogen-Doped Mesoporous Carbon for Supercapacitor Application. C - Journal of Carbon Research 2018, 4, 20.

(39) Le Bail, A. Whole Powder Pattern Decomposition Methods and Applications: A Retrospection. Powder Diffr. 2005, 20, 316−326.
(40) Rodríguez-Carvajal, J. Recent Advances in Magnetic Structure Determination by Neutron Powder Diffraction. Phys. B 1993, 192, 55−69.
(41) Roisnel, T.; Rodríguez-Carvajal, J. WinPLOTR: A Windows Tool for Powder Diffraction Analysis. Mater. Sci. Forum 2001, 378- 381, 118.
(42) O'Neill, L. ICDD Annual Spring Meetings. Powder Diffr. 2013, 28, 137−148.
(43) Schneider, C. A.; Rasband, W. S.; Eliceiri, K. W. NIH Image to ImageJ: 25 Years of Image Analysis. Nat. Methods 2012, 9, 671−675.
(44) Beda, A.; Villevieille, C.; Taberna, P.-L.; Simon, P.; Matei Ghimbeu, C. Self-Supported Binder-Free Hard Carbon Electrodes for Sodium-Ion Batteries: Insights into Their Sodium Storage Mechanisms. J. Mater. Chem. A 2020, 8, 5558−5571.
(45) Beda, A.; Taberna, P.-L.; Simon, P.; Matei Ghimbeu, C. Hard Carbons Derived from Green Phenolic Resins for Na-Ion Batteries. Carbon 2018, 139, 248−257.
(46) Grimes, R. W.; Fitch, A. N. Thermal Decomposition of Cobalt(II) Acetate Tetrahydrate Studied with Time-Resolved Neutron Diffraction and Thermogravimetric Analysis. J. Mater. Chem. 1991, 1, 461−468.
(47) Wanjun, T.; Donghua, C. Mechanism of Thermal Decomposition of Cobalt Acetate Tetrahydrate. Chemical Papers 2007, 61, 329−332.
(48) Ghimbeu, C. M.; Sopronyi, M.; Sima, F.; Delmotte, L.; Vaulot, C.; Zlotea, C.; Paul-Boncour, V.; Le Meins, J.-M. One-Pot Laser- Assisted Synthesis of Porous Carbon with Embedded Magnetic Cobalt Nanoparticles. Nanoscale 2015, 7, 10111−10122.
(49) Liu, X.; Yi, R.; Zhang, N.; Shi, R.; Li, X.; Qiu, G. Cobalt Hydroxide Nanosheets and Their Thermal Decomposition to Cobalt Oxide Nanorings. Chem. - Asian J. 2008, 3, 732−738.
(50) Sun, D.; He, L.; Chen, R.; Lin, Z.; Lin, S.; Xiao, C.; Lin, B. The Synthesis, Characterization and Electrochemical Performance of Hollow Sandwich Microtubules Composed of Ultrathin Co_3O_4 Nanosheets and Porous Carbon Using a Bio-Template. J. Mater. Chem. A 2018, 6, 18987−18993.
(51) Hadjiev, V. G.; Iliev, M. N.; Vergilov, I. V. The Raman Spectra of Co_3O_4. J. Phys. C: Solid State Phys. 1988, 21, L199−L201.
(52) Nita, C.; Fullenwarth, J.; Monconduit, L.; Le Meins, J.-M.; Fioux, P.; Parmentier, J.; Matei Ghimbeu, C. Eco-Friendly Synthesis of SiO_2 Nanoparticles Confined in Hard Carbon: A Promising Material with Unexpected Mechanism for Li-Ion Batteries. Carbon 2019, 143, 598−609.

(53) Yan, H.; Bai, J.; Liao, M.; He, Y.; Liu, Q.; Liu, J.; Zhang, H.; Li, Z.; Wang, J. One-Step Synthesis of Co_3O_4/Graphene Aerogels and Their All-Solid-State Asymmetric Supercapacitor. Eur. J. Inorg. Chem. 2017, 2017, 1143−1152.
(54) Voorhees, P. W. The Theory of Ostwald Ripening. J. Stat. Phys. 1985, 38, 231−252.
(55) Guan, C.; Sumboja, A.; Wu, H.; Ren, W.; Liu, X.; Zhang, H.; Liu, Z.; Cheng, C.; Pennycook, S. J.; Wang, J. Hollow Co_3O_4 Nanosphere Embedded in Carbon Arrays for Stable and Flexible Solid-State Zinc−Air Batteries. Adv. Mater. 2017, 29, 1704117.
(56) Platek, A.; Nita, C.; Ghimbeu, C. M.; Frąckowiak, E.; Fic, K. Electrochemical Capacitors Operating in Aqueous Electrolyte with Volumetric Characteristics Improved by Sustainable Templating of Electrode Materials. Electrochim. Acta 2020, 338, 135788.
(57) Chmiola, J. Anomalous Increase in Carbon Capacitance at Pore Sizes Less Than 1 Nanometer. Science 2006, 313, 1760−1763.
(58) Zhao, Y.; Liu, Y.; Du, J.; Zhang, X.; Zhou, J.; Li, X.; Wu, C.; Zhu, Z.; Xie, E.; Pan, X. Facile Synthesis of Interconnected Carbon Network Decorated with Co_3O_4 Nanoparticles for Potential Supercapacitor Applications. Appl. Surf. Sci. 2019, 487, 442−451.
(59) Abouali, S.; Akbari Garakani, M.; Zhang, B.; Xu, Z.-L.; Kamali Heidari, E.; Huang, J.; Huang, J.; Kim, J.-K. Electrospun Carbon Nanofibers with in Situ Encapsulated Co_3O_4 Nanoparticles as Electrodes for High-Performance Supercapacitors. ACS Appl. Mater. Interfaces 2015, 7, 13503−13511.
(60) Xie, L.-J.; Wu, J.-F.; Chen, C.-M.; Zhang, C.-M.; Wan, L.; Wang, J.-L.; Kong, Q.-Q.; Lv, C.-X.; Li, K.-X.; Sun, G.-H. A Novel Asymmetric Supercapacitor with an Activated Carbon Cathode and a Reduced Graphene Oxide−Cobalt Oxide Nanocomposite Anode. J. Power Sources 2013, 242, 148−156.
(61) Xie, L.; Su, F.; Xie, L.; Li, X.; Liu, Z.; Kong, Q.; Guo, X.; Zhang, Y.; Wan, L.; Li, K.; Lv, C.; Chen, C. Self-Assembled 3D Graphene- Based Aerogel with Co_3O_4 Nanoparticles as High-Performance Asymmetric Supercapacitor Electrode. ChemSusChem 2015, 8, 2917− 2926.
(62) Iqbal, M. Z.; Haider, S. S.; Zakar, S.; Alzaid, M.; Afzal, A. M.; Aftab, S. Cobalt-Oxide/Carbon Composites for Asymmetric Solid- State Supercapacitors. Mater. Res. Bull. 2020, 131, 110974.
(63) Wu, F.-C.; Tseng, R.-L.; Hu, C.-C.; Wang, C.-C. Effects of Pore Structure and Electrolyte on the Capacitive Characteristics of Steamand KOH-Activated Carbons for Supercapacitors. J. Power Sources 2005, 144, 302−309.
(64) Han, L.; Xu, Z.; Wu, J.; Guo, X.; Zhu, H.; Cui, H. Controllable Preparation of Graphene/MnO_2/Co_3O_4 for Supercapacitors. J. Alloys Compd. 2017, 729, 1183−1189.

(65) Yan, J.; Wei, T.; Qiao, W.; Shao, B.; Zhao, Q.; Zhang, L.; Fan, Z. Rapid Microwave-Assisted Synthesis of Graphene Nanosheet/ Co_3O_4 Composite for Supercapacitors. Electrochim. Acta 2010, 55, 6973−6978.
(66) Largeot, C.; Portet, C.; Chmiola, J.; Taberna, P.-L.; Gogotsi, Y.; Simon, P. Relation between the Ion Size and Pore Size for an Electric Double-Layer Capacitor. J. Am. Chem. Soc. 2008, 130, 2730−2731.
(67) Yang, C.-C.; Hsu, S.-T.; Chien, W.-C. All Solid-State Electric Double-Layer Capacitors Based on Alkaline Polyvinyl Alcohol Polymer Electrolytes. J. Power Sources 2005, 152, 303−310.
(68) Funaki, T.; Hikihara, T. Characterization and Modeling of the Voltage Dependency of Capacitance and Impedance Frequency Characteristics of Packed EDLCs. IEEE Trans. Power Electron. 2008, 23, 1518−1525.
(69) Beda, A.; Le Meins, J.-M.; Taberna, P.-L.; Simon, P.; Matei Ghimbeu, C. Impact of Biomass Inorganic Impurities on Hard Carbon Properties and Performance in Na-Ion Batteries. Sustainable Materials and Technologies 2020, 26, e00227.
(70) Shi, F.; Li, L.; Wang, X.; Gu, C.; Tu, J. Metal Oxide/Hydroxide- Based Materials for Supercapacitors. RSC Adv. 2014, 4, 41910−41921.